Using Collision Cones to Asses Biological Deconfliction Methods

Natalie Brace

A thesis submitted in partial fulfillment of the
requirements for the degree of

Master of Science in Aeronautics & Astronautics

University of Washington

2014

Reading Committee:

Kristi Morgansen, Chair

Mehran Mesbahi

Program Authorized to Offer Degree:
William E. Boeing Department of Aeronautics & Astronautics

University of Washington

Abstract

Using Collision Cones to Asses Biological Deconfliction Methods

Natalie Brace

Chair of the Supervisory Committee:
Associate Professor Kristi Morgansen
Aeronautics & Astronautics

For autonomous vehicles to navigate the world as efficiently and effectively as biological species, improvements are needed in terms of control strategies and estimation algorithms. Reactive collision avoidance is one specific area where biological systems outperform engineered algorithms. To better understand the discrepancy between engineered and biological systems, a collision avoidance algorithm was applied to frames of trajectory data from three biological species (*Myotis velifer, Hirundo rustica,* and *Danio aequipinnatus*). The algorithm uses information that can be sensed through visual cues (relative position and velocity) to define collision cones which are used to find a safe velocity that requires minimal deviation from the original velocity for each individual agent in conflict. Two- and three-dimensional versions of the algorithm with constant and maximum speed velocity requirements were considered. The obstacles provided to the algorithm were determined by the sensing range in terms of either metric or topological distance. The calculated velocities showed good correlation with observed velocities over the range of sensing parameters, indicating that the algorithm is a good basis for comparison and could potentially be improved with further study.

TABLE OF CONTENTS

Page

LIST OF FIGURES

ACKNOWLEDGMENTS

The author would like to express appreciation to her advisor, Kristi Morgansen, who provided encouragement and guidance throughout the course of this work, to Ty Hedrick, who provided consultation on the behavior of (unladen) swallows, as well as to the graduate students of the Nonlinear Dynamics and Controls Laboratory, who provided assistance and camaraderie. She would also like to thank her parents, for their love and for the academic opportunities they afforded her, and her husband Eric, for his love, support, and simply for being her favorite.

Chapter 1

INTRODUCTION

An increasingly wide array of unmanned vehicles are becoming available with a diverse set of form factors and ever expanding capabilities. To fully utilize the enhanced control authority and sensing that comes with these improvements to effectively and safely navigate the world will require improved control algorithms and estimation strategies capable of real-time path planning through changing conditions and unexpected obstacles. Many biological systems display a remarkable ability to perform such tasks seemingly effortlessly, so we look to their example to discern the principles underlying the highly effective reactive collision avoidance abilities developed through evolution.

Biological models have been developed to describe the emergence of self-organization and other collective behavior in large groups of animals, including schooling and shoaling fish, flocking birds, swarming insects, and herding land animals [1]. Certain models provide insight into animals' sensing or cognitive limitations: animals in a large group appear to only take into account some smaller number of nearby animals. The membership of and interactions within these smaller groups may be dependent on a metric distance, for example the zonal model of shoaling fish [2], or a topological distance, as in the model of swarming starlings [3]. Models of perception have also been developed to investigate the use of optic flow in birds [4] and bats [5] and even visual tracking to aid collision avoidance in insects [6]. Typically these models begin with extensive observations of the species and develop into theories that explain or reproduce the behavior - the study here takes the opposite approach, by starting with an engineered algorithm and determining how well it correlates to observed behavior.

The study of systems theory with respect to biological behavior, and vice versa, has been a popular topic for many years. A particle model was used to produce realistic flocking animations by basing the behavior of boids (bird-oid objects) upon the requirements of

collision avoidance, velocity matching, and flock cohesion [7]. Consensus decision-making of social groups has been studied to investigate decision making among a group [8, 9]. Specifically, the social behavior of schooling fish in response to predators was considered [10] and, to further facilitate this line of research, robotic fish and a feedback control system relative to a collocated shoal of live fish have been developed [11]. Chazelle introduces 'Natural Algorithms' to describe collective behavior through its own calculus, taking elements from dynamic and networked systems and statistical mechanics while maintaining a general framework [12, 13]. Not limited to studies of collective behavior, Karaman and Frazzoli developed a theoretical framework to investigate the collision avoidance problem solved by birds when navigating a forest at high speed and found a critical speed below which a conflict-free path could be flown indefinitely [14].

Dynamic collision avoidance for autonomous vehicles is challenging and is an ongoing topic of research. Preventing vehicles from coming too close to static objects in a cluttered environment is feasible, however it becomes much more challenging when dynamic obstacles are introduced since offline or global path planning techniques can no longer be applied. A wide array of methods have been applied to the problem of conflict resolution, i.e., the act of identifying and avoiding future collisions, with varying degrees of centralization and safety and convergence guarantees [15]. Centralization refers to the distribution (or lack thereof) of information and processing: a centralized system processes global information to perform conflict resolution for all agents at a single location, whereas each agent in a distributed system determines its individual collision avoidance strategy using only local information. A distributed system falls between those extremes, with each agent processing global information individually. Prescribed maneuvers (e.g., always turn left) provide a simple rule-based approach for a small number of vehicles, but can become prohibitively complex for a large number of vehicles; considering only the most imminent collisions can simplify the problem and promote efficiency at the cost of maintaining separation distance [16]. Force field methods treat goals and obstacles as charged particles: goals are oppositely charged (attractive) and obstacles are similarly charged (repulsive). These forces also give rise to artificial potential field and navigation function (the latter is guaranteed smooth with no local minima) methods that follow the decreasing gradient toward the goal while

avoiding obstacles. A decentralized navigation function was layered with a swirling function (preventing symmetries and saddle points) to provide guaranteed collision avoidance for a pair of vehicles in [17]. Optimization methods seek to find the best collision-free path with respect to some cost function. The optimal solution can be found for all cooperative agents using a centralized approach [18] or for individual agents using a decentralized [19] or distributed [20, 21] approach.

A subset of the conflict resolution algorithms that reflect biological methods include model predictive control, bug-family algorithms, and certain sensor-based techniques. A model predictive control strategy plans a safe path based on a goal for a limited time horizon, executes the first step of that plan, collects new information, checks for differences between planned and actual outcomes, and repeats the process [22]. This technique is not unlike how biological species process information [23], however it typically involves optimizing a trajectory with respect to a finely tuned cost function. Bug algorithms on the other hand utilize a seemingly straightforward strategy requiring minimal sensing information: head toward the target until an obstacle is detected, then follow its boundary until the path to the target is clear again [24]. Sensor-based techniques rely on knowledge of some region of space near the autonomous agent that can be sensed and used for planning; velocity obstacles fall into this category, using relative position and speed of other agents and obstacles to discriminate safe and unsafe velocity vectors [25, 26].

The Distributed Reactive Collision Avoidance (DRCA) algorithm uses collision cones, a version of velocity obstacles, to provide safe paths for an arbitrary number of agents [21]. The algorithm detects conflicts (future collisions) by checking if the current velocity falls within a collision cone. If a conflict is detected, the safe velocity nearest the original velocity is found and implemented in a deconfliction maneuver. In biological terms, this implementation assumes an animal will continue in one direction until something in its environment forces it to change, and then it will deviate as little as possible from its original path. The calculations are performed for each agent individually and require only information that can be obtained from visual cues: velocity, bearing, and range of other agents. The distributed nature, lack of complicated cost function, and limited sensing requirements of this algorithm make it a good candidate for comparison with biological species. The use of velocity

obstacles, provides a biological basis for this comparison, since both birds and bats have been found to use velocity cues to solve the opposite problem of target tracking by applying a version of constant bearing, decreasing range techniques [27, 28]. In this work, the three species providing the biological data for comparison to the DRCA algorithm are agile and social animals sampled from bats (*Myotis velifer*), birds (*Hirundo rustica*), and fish (*Danio aequipinnatus*).

1.1 Research Contributions

The comparative analysis presented in this thesis provides an initial step in informing improvements of engineered deconfliction algorithms based on biological principles. A limited version of this analysis was performed previously by Boardman et al. [29], however in that study the three-dimensional trajectory data was flattened to two dimensions prior to performing conflict detection which resulted in a large number of 'phantom' conflicts. The present work is based on the same biological data, but performs conflict detection and velocity comparisons in three dimensions, providing a more accurate assessment of the correlation. To more accurately capture the full perception of the animals, three dimensional extensions to the DRCA deconfliction maneuvers and models of static obstacles were developed. This study also accounts for the inherent delay between perception and reaction by comparing the algorithmically prescribed velocity to observed velocities in the next time step and at the animal's reaction time. The results for all species at their reaction times indicate a relatively good correlation with the algorithm.

1.2 Thesis Organization

This thesis is organized as follows. Chapter 2 provides background on the three biological species and details of the biological models used for characterizing their sensing range. Chapter 3 describes the components of the DRCA algorithm applicable to the analysis, including the original two-dimensional constant and variable speed versions of the deconfliction maneuver and three-dimensional extensions thereof, and a description of how static obstacles were modeled. Chapter 4 presents the results of the comparison as well as additional metrics that were applied to the available trajectory data. Chapter 5 contains final remarks and suggestions for future work.

Chapter 2

BIOLOGICAL BACKGROUND

The species used for comparison in this study were chosen due to their agile maneuvering capabilities and social nature. The available data sets provide both dynamic obstacles, in the form of multiple moving animals, and static obstacles, such as silos, barns, a hanging vine, and fish tank walls present within the observation volume. The animals are probably not paying attention to all of the objects around them, so two models are presented, based on metric and on topological distance, for selecting an influential subset of objects in each scene to use for the collision avoidance calculations.

2.1 Biological Species

2.1.1 Emerging Cave Bats

Myotis velifer are bats that roost in colonies found in caves and tunnels. Each night they emerge in small groups after sunset [30]. They are insectivores and use echolocation as their primary means of sensing, although one study suggests that vision may also play a role in navigation [5]. An average bat in this species is 0.1 meters long with a wingspan of 0.3 meters, weighs 12 grams, and has a cruising speed of 5.5-6.6 meters per second [31, 30].

Trajectory data were collected for 9 seconds at 131.5 frames per second as a group of 20 bats emerged from their cave on the Bamberger Ranch in Texas. Each bat was in view for approximately 1.9 seconds with a maximum of 10 bats in view at any one time. In addition to other animals, there were also two static obstacles in their flight path: a pole 1.6 meters tall and a vine 0.2 meters wide extending from the ground to the forest canopy. The bats' trajectories and the static objects are depicted in Figure 2.1.

The cave bats were filmed in low light using three mid-infrared FLIR SC8000 cameras at a resolution of 1024 x 1024 pixels [29]. Calibration was performed for both bats and swallows by passing a 1 meter long reference object through the shared field of view and applying

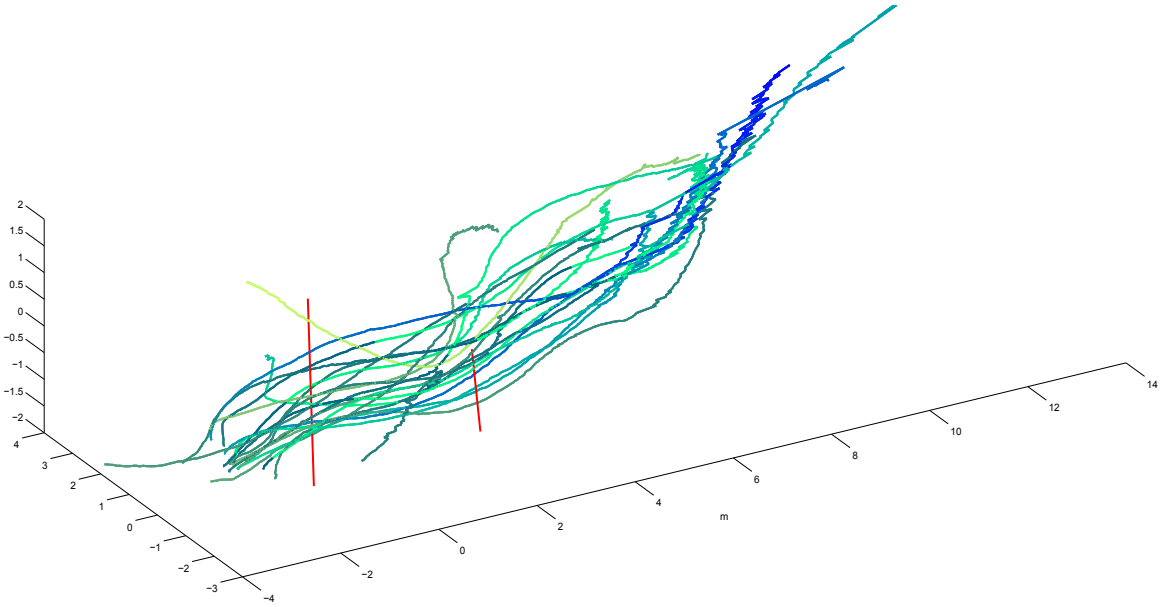

Figure 2.1: Trajectories of 20 bats emerging from their cave (blue-green lines) and static obstacles in their path (red lines). Trajectories of the same color were present concurrently.

a structure-from-motion algorithm. Correspondences between the views were made using semi-automated tracking tools and the three-dimensional trajectories were generated using least squares. The bats were filmed by the Kunz Bat Lab, and the post-processing was done by the Image and Video Computing Group, both at Boston University.

2.1.2 Maneuvering Barn Swallows

Hirundo rustica are semi-colonial passerine birds that tend to nest in or around human stuctures such as barns. Barn swallows are capable fliers, interacting with the elements of their environment as well as with each other and foraging for insects. They are typically 0.18 meters long with a wingspan of 0.32 meters, weigh 20 grams, and have an average cruising speed of 8 meters per second [32, 33]. Data was collected for the swallows near a nesting site at a farm in Yanceyville, North Carolina. Each scene was recorded for 4.75 seconds at 100 frames per second. The birds were interacting with three silos and two rooflines, the latter of which provided both an obstacle and a perch. Trajectories of the swallows and the static obstacles are shown in Figure 2.2.

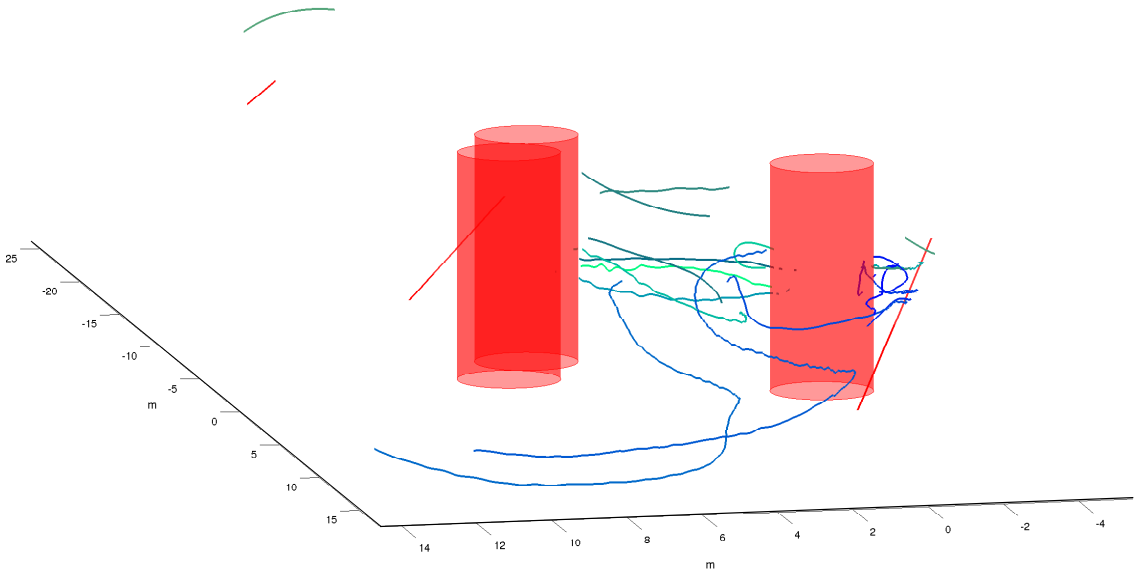

Figure 2.2: Trajectories of 23 barn swallows (blue-green lines) and static obstacles, including 6 meter tall silos (red cylinders) and building eaves (red lines).

The swallows were filmed using three IDT N5 cameras outfitted with Nikon 20 mm f/28 AF lenses at a resolution of 2336 x 1728 pixels [29]. Calibration was performed using the same method as the for the bats. Objects were tracked and triangulated between two or three of the cameras to produce the three dimensional data [34]. The data were smoothed using a spline with error tolerance taken from the reconstruction error (based on distance and quality of tracking and calibration). The barn swallow data were collected by the Hedrick Lab at the University of North Carolina at Chapel Hill.

2.1.3 Shoaling Fish

Danio aequipinnatus are small freshwater fish found in loose groups in rivers and streams. The animals in the trial were circa 0.053 meters in length with a circumference of approximately 0.15 body lengths (8 millimeters) and weighed 1.7 grams [8].

The fish were filmed in a square tank measuring 1.8 meters per side and 1 meter deep.

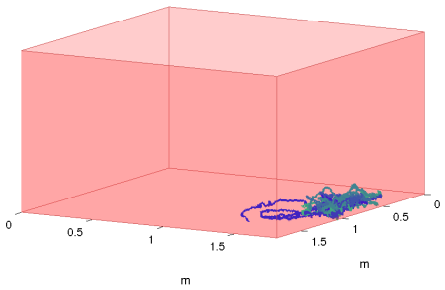

Figure 2.3: Untrained giant danio prior to the food stimulus.

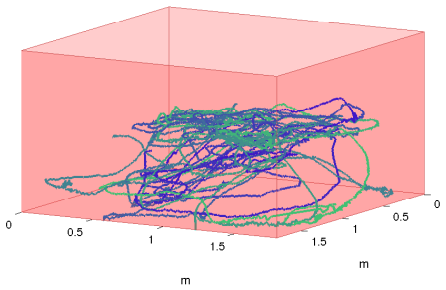

Figure 2.4: Trained giant danio after to the food stimulus.

Figures 2.3-2.4: Trajectories of 15 giant danio (blue-green lines) depicted within their fish tank (red surfaces).

During each recording there were 15 fish in the tank which were some combination of naive fish and those trained to respond to a food stimulus. Specifically, during the two weeks prior to the data collection, the trained fish were exposed to red lights when food was delivered to the tank. The recordings were captured at 30 frames per second and separated into 1 minute segments before, during, and after the food cue [8]. To minimize the variables for the current study, only data sets with all untrained (0-15) or trained (15-0) fish before and after the food cue were used for analysis; the trajectories are shown in Figures 2.3 and 2.4.

The movements of the fish within the tank were captured by four Panasonic x300 digital palmcorder cameras [8]. The video data was processed into three dimensional trajectories using the software package tracker3D. Camera calibration was done using a grid placed on the top and bottom of the tank. The fish data was collected at the University of Washington in the Birdfish Lab under the direction of Julia Parrish.

2.2 Behavioral Models

Mathematical models are tools used to gain an understanding of the mechanisms underlying self-organization observed in many large groups of animals, especially fish and birds. Two such models classify the type of interaction of an individual animal with nearby animals as

defined by function of metric or topological distance.

2.2.1 Metric Distance

Also called a zonal model, this method uses the radial distance from an animal to classify its interaction with nearby neighbors as repulsive, aligning, or attractive [2] (Figure 2.5). The repulsive zone is closest to the focus animal and extends from its center of mass to a radius d_r. The focus will move away from any animals within d_r. The alignment or neutral zone extends from d_r to d_{align}. In the case of alignment, the focus will seek to align its heading to those of other animals in this zone. An alternative interpretation is that this zone is a fuzzy area between repulsion and attraction due to imprecise distance sensing. Beyond the alignment zone but within the sensing range, d_a, of the animal is the zone of attraction. The focus will be drawn towards animals between d_{align} and d_a. Animals beyond the attraction zone are not considered by the focus animal.

There are multiple variations of this model, the simplest of which will be used for the following analysis. The zones can be shaped as ellipsoids with the major axes aligned with the heading of the focus animal. Aditionally, a cone representing the animal's blind spot may be removed from directly behind the focus animal. In the analysis performed for this study, a constant d_a was used to define the maximum sensing range within which potential collisions are, presumably, detected and avoided. To determine the influence of metric distance on the collision avoidance behavior of the animals, a range of d_a values were considered for each species.

2.2.2 Topological Distance

The topological distance is described by relative proximity of animals to the focus animal - this distance is measured in fish/birds/bats rather than meters, as shown in Figure 2.6. The number of animals under consideration remains constant regardless of the radial distance from the focus to nearby animals. Thus, the cognitive load remains relatively constant for any density of the group, and the animal does not become overwhelmed if there is a contraction of the group, for instance. The number of influential neighbors has been shown

to be important in both flocking birds [3] and schooling fish [2]; there is a lack of information in the literature for bats.

Comparison of a mathematical model to empirical data of starling murmurations swarming by the thousands above their nesting sites indicated that the number of influential nearest neighbors was more important than metric range. The model best matches the data when six to seven influential neighbors are considered. This result is consistent with the ability of pigeons to track objects in sets of fewer than seven [35].

For a model of schooling fish, Viscideo et al. showed a relationship between the number of influential neighbors and group size and that group size is in turn related to population size [2]. The relationship between group,which is a smaller cluster of animals within the entire population (here defined as within 5 body lengths of each other), and population size is given by an exponential, but the ratio is approximately one-to-one until the population exceeds twenty fish. Viscideo et al. provide a linear relationship for the group size G as a function of the number of influential neighbors, N, which can be inverted to obtain the relationship $N = (G + 6.69)/3.10$. Using $G = 15$, the number of influential neighbors is $N = 7.00$.

To determine the influence of topological distance on the collision avoidance behavior of the animals, a range of number of nearest neighbors, N, were considered for each species.

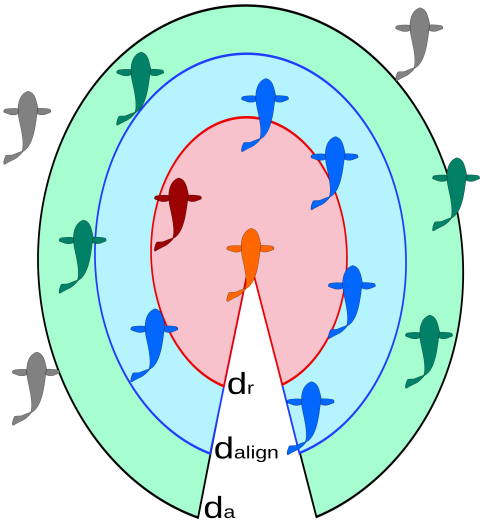

Figure 2.5: In the zonal model, radii around the focus animal (orange) define the type of interaction with other animals: those within d_r (red) are repulsive, between d_r and d_{align} (blue) are neutral or aligning, and between d_{align} and d_a (green) are attractive. Animals outside of d_a (gray) are not sensed or are ignored.

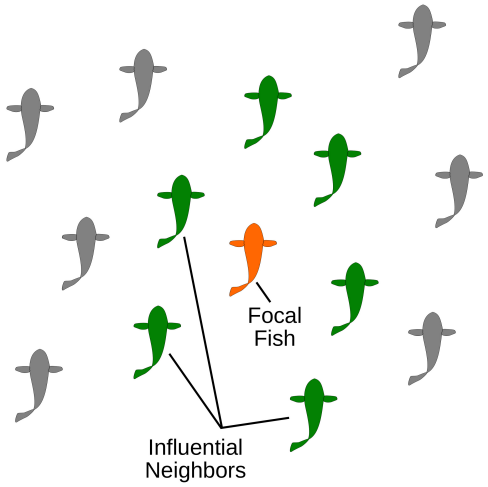

Figure 2.6: In the topological distance model, a set of animals nearest the focal animal (orange) are considered influential neighbors (green). Animals outside this inner grouping (gray) are not considered by the focal animal.

Chapter 3

COLLISION AVOIDANCE

Avoiding obstacles is a common goal of mobile systems, both biological and engineered. The DRCA algorithm is based on two layers: a deconfliction maneuver that brings vehicles out of conflict by choosing a safe velocity nearest to the current velocity and a deconfliction maintenance maneuver that ensures conflicts do not occur in the future [21]. The algorithm begins by checking to see if a conflict exists. If there is a conflict, a deconfliction maneuver uses the current velocity and position information of the focus agent and all other agents and static obstacles within sensing distance to find the safe velocity that requires minimum deviation from the original velocity. If there is not a conflict, the deconfliction maintenance maneuver would use the same situational information to augment an underlying controller to allow the agent to follow a desired course as closely as possible without generating any new conflicts; the maintenance maneuver is not presented here. The maneuvers are calculated in velocity space, which can present a challenge when agents are interacting with static objects, so models were developed to strategically generate appropriate static obstacles.

3.1 Conflict Definition and Detection

Impending collisions must first be perceived before they can be avoided, so the first step is detecting conflict. A *collision* occurs when two objects come within a specified minimum separation distance, $d_{sep,ij}$. The minimum separation distance, $d_{sep,i}$, describes the radius of a sphere around object i; the minimum separation distance for two objects i and j is then $d_{sep,ij} = d_{sep,i} + d_{sep,j}$. Thus a collision between objects i and j separated by the relative position vector $\mathbf{r}_{ij} = \mathbf{r}_j - \mathbf{r}_i$ happens when $\|\mathbf{r}_{ij}\| < d_{sep,ij}$.

A *conflict* occurs when two objects will eventually enter a collision if their current velocities are maintained. The set of velocities that will eventually cause a vehicle to collide with another can be described by a collision cone; formally, the set of velocity obstacles for

agent i caused by agent j is the set of velocities $\mathbf{v}_i$ such that $(\mathbf{v}_i - \mathbf{v}_j)t \in B(\mathbf{r}_{ij}, d_{sep,ij})$ for some time $t > 0$, where $B(\mathbf{x}, d)$ is a ball of radius d centered at $\mathbf{x}$. The collision cone is constructed in velocity space with its vertex at the velocity of the obstacle, $\mathbf{v}_j$, and axis in the direction of the relative velocity vector, $\mathbf{r}_{ij}$; objects i and j are in conflict if $\mathbf{v}_i$ falls within the collision cone generated by $\mathbf{v}_j$. The half-angle of the collision cone, α, is calculated from the distance and combined required separation between two objects by

$$\alpha = \arcsin \frac{d_{sep,ij}}{\|\mathbf{r}_{ij}\|}. \tag{3.1}$$

Defining β as the angle between the relative position and relative velocity vectors, that is $\beta = \angle\mathbf{r}_{ij} - \angle\mathbf{v}_{ij}$ where $\mathbf{v}_{ij} = \mathbf{v}_i - \mathbf{v}_j$, the criteria for conflict is simply $\alpha < \beta$ [21]. The collision cone geometry for objects in and out of conflict is shown Figures 3.1 and 3.2. Conflict detection is always done in three dimensions.

3.2 Deconfliction Maneuvers

When a conflict is detected, an optimal safe (i.e., conflict-free), feasible velocity, $\mathbf{v}_i^*$, is calculated. This velocity is selected by the algorithm to be outside of all collision cones (making it safe) and to require the smallest deviation (in the sense of a L_2 norm) from the current velocity $\mathbf{v}_i$ (making it optimal) while satisfying certain speed constraints dependent on the maneuver type (making it feasible). The constant speed maneuver requires the magnitude of the velocity vector to remain constant, so the new velocity represents a change only in the heading. The variable speed maneuver requires that the velocity remain below some maximum speed, allowing for changes in both speed and direction. For both maneuvers, the potential optima $\mathbf{v}_i'$ are found, put in order from smallest to largest deviation from the original velocity $\mathbf{v}_i$, and then each $\mathbf{v}_i'$ is checked for conflicts. Due to the ordering, the first conflict-free velocity $\mathbf{v}_i'$ is optimal. The original DRCA algorithm calculates deconfliction maneuvers using only two dimensions, which limits the number of potential optimal velocity vectors to a finite set of points at the intersections of the edges of collision cones and speed requirements that can easily be calculated algebraically. A three dimensional extension of the deconfliction maneuver was developed to better accommodate the out-of-plane components of perception and movement seen in flying and swimming animals; the potential

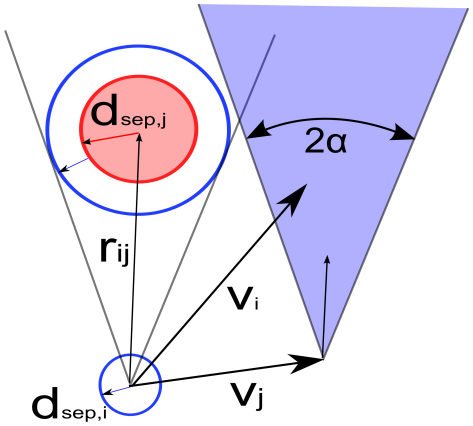

Figure 3.1: Depiction of the geometry of a collision cone (blue shaded area) in velocity space for focus agent i that is in conflict with agent j. The vertex of the collision cone is the velocity vector of the other agent, $\mathbf{v}_j$, the axis is in the direction of the relative position vector, $\mathbf{r}_{ij}$, and the cone angle, α, is determined in (3.1) by the distance between the two agents, $\|\mathbf{r}_{ij}\|$, and the required separation distance, $d_{sep,i} + d_{sep,j}$.

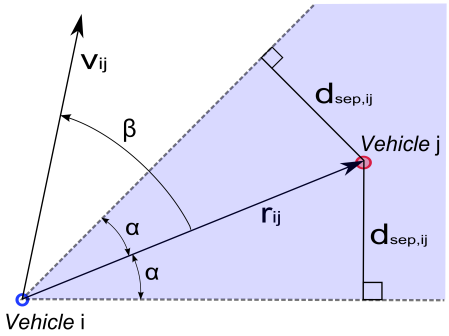

Figure 3.2: Depiction of a collision cone for agents that are not in conflict: $\alpha < \beta$ indicating that $\mathbf{v}_{ij}$ falls outside the collision cone (adapted from [21]).

three-dimensional optima are found using numerical methods. To allow for comparison of three-dimensional trajectory data with the original algorithm, the data were flattened to a plane in a global or body-fixed coordinate system.

3.2.1 Constant Speed

The potential optimal solutions $\mathbf{v}_i'$ lie on the circle or spherical shell of constant speed where it is intersected by one or more collision cones. Mathematically, the speed constraint is $\|\mathbf{v}_i'\| = r$ where $r = v_c$ is the required speed. To calculate the potential optima for each collision cone, first a unit vector along the side of the collision cone lying in the $\mathbf{r}_{ij} - \mathbf{v}_{ij}$ plane is constructed as

$$\hat{\mathbf{c}} = \hat{\mathbf{r}}_{ij} \cos\alpha + \left(\frac{\mathbf{q} \times \hat{\mathbf{r}}_{ij}}{\|\mathbf{q}\|} \right) \sin(\alpha), \tag{3.2}$$

where $\mathbf{q} = \mathbf{r}_{ij} \times \mathbf{v}_{ij}$ and $\hat{\mathbf{r}}_{ij} = \mathbf{r}_{ij}/\|\mathbf{r}_{ij}\|$ denotes a unit vector in the direction of $\mathbf{r}_{ij}$. In two dimensions, (3.2) reduces to $\hat{\mathbf{c}} = R(\pm\alpha)\hat{\mathbf{r}}_{ij}$ where $R \in SO(2)$ is a rotation matrix. Then the potential optima in the two-dimensional maneuver are on each side of a collision cone where it meets the circle of constant speed, or at

$$\mathbf{v}_i' = \mathbf{v}_j - a\hat{\mathbf{c}}, \qquad a = \hat{\mathbf{c}}^T\mathbf{v}_j \pm \sqrt{(\hat{\mathbf{c}}^T\mathbf{v}_j)^2 - \mathbf{v}_j^T\mathbf{v}_j + \mathbf{v}_i^T\mathbf{v}_i}.$$

Locations of potential two-dimensional optima are shown in Figure 3.3.

Remark: The collision cone geometry also provides a method of intercepting another agent: selecting the velocity at the intersection of the collision cone axis with the circle of constant speed is equivalent to a constant bearing, decreasing range strategy.

In three dimensions, the intersection of a cone and a sphere is a curve or ring, shown in Figure 3.4. The possible optimal solutions are at either the nearest point to $\mathbf{v}_i$ on one ring or at the intersection of two rings. To find these locations using numerical tools in Matlab, the problem was formulated as a minimization problem using Lagrange multipliers with constraint equations given by the surfaces of the cone and spherical shell. A basic formulation of a minimization problem seeks to find the component values of $\mathbf{x}$ such that the scalar cost function $L(\mathbf{x})$ is minimized subject to one or more scalar constraints $\mathbf{g}(\mathbf{x}) = \mathbf{0}$. These components are combined with Lagrange multipliers $\boldsymbol{\lambda}$ to form the Hamiltonian

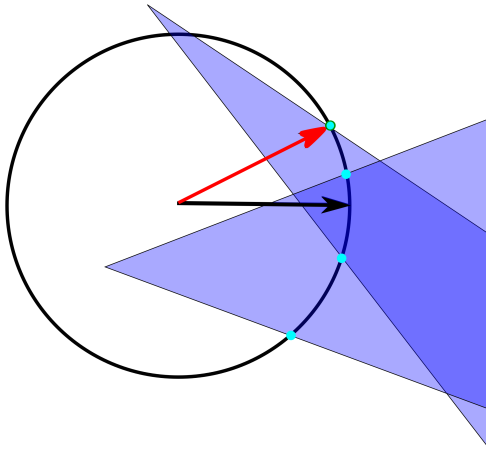

Figure 3.3: Depiction of the two dimensional constant speed maneuver showing potential optima (cyan circles).

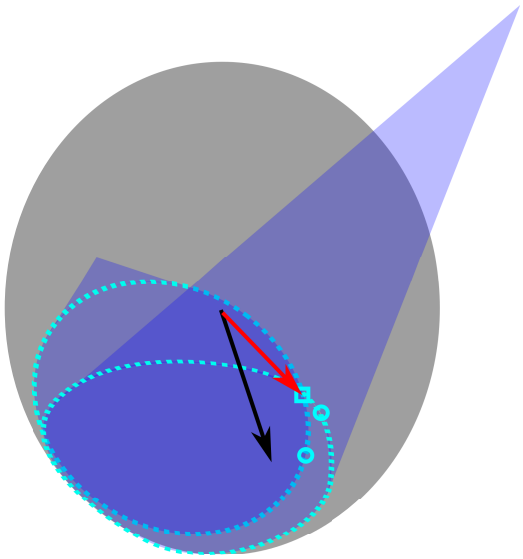

Figure 3.4: Depiction of the three dimensional constant speed maneuver showing intersections where potential optima lie (cyan dotted lines) and potential optima on one cone (cyan circles) and two cones (cyan square).

Figures 3.3-3.4: The two- and three-dimensional constant speed maneuvers find optimal safe velocities (red) nearest to the original velocity (black) at the intersection of the collision cones (blue) and the circle (black) or sphere (gray) of constant speed.

$H(\mathbf{x}, \lambda) = L(\mathbf{x}) + \boldsymbol{\lambda}^T \mathbf{g}(\mathbf{x})$. Then the necessary conditions for a minimum of the cost function are achieved when the partial derivatives of the Hamiltonian with respect to $\mathbf{x}$ and λ are zero. Thus, the problem of finding the nearest point along the intersection of a single cone and the sphere can be stated as:

$$\min_{\mathbf{v}_i'} L(\mathbf{v}_i') = \|\mathbf{v}_i - \mathbf{v}_i'\|^2$$

subject to

$$g_1(\mathbf{v}_i') = \mathbf{p}^T Q_{sphere} \mathbf{p} = 0, \text{ and}$$
$$g_2(\mathbf{v}_i') = \mathbf{p}^T Q_{cone} \mathbf{p} = 0$$

where the constraint equations are the surfaces of the sphere and cone written using vector notation with $\mathbf{p} = \begin{bmatrix} \mathbf{v}_i' & 1 \end{bmatrix}$ and $Q_{surface} \in \mathbb{R}^{4x4}$ describes the surface of the cone or sphere; an explanation of matrix representations of quadric surfaces, specifically spheres and cones, is provided in Appendix A.

The solution is found by defining the Hamiltonian function as

$$H(\mathbf{v}_i', \lambda_1, \lambda_2) = L + \lambda_1 g_1 + \lambda_2 g_2$$

and setting the partial derivitives of the Hamiltonian with respect to the components of $\mathbf{v}_i' = [x \ y \ z]$ and the Lagrange multipliers λ_1, λ_2 equal to zero:

$$\frac{\partial H}{\partial x_s} = 0 = 2x - 2v_{i,x} + \lambda_1(2A_1x + 2D_1y + 2F_1z + 2G_1) + \lambda_2(2A_2x + 2D_2y + 2F_2z + 2G_2)$$
$$\frac{\partial H}{\partial y_s} = 0 = 2y - 2v_{i,y} + \lambda_1(2D_1x + 2B_1y + 2E_1z + 2H_1) + \lambda_2(2D_2x + 2B_2y + 2E_2z + 2H_2)$$
$$\frac{\partial H}{\partial z_s} = 0 = 2z - 2v_{i,z} + \lambda_1(2F_1x + 2E_1y + 2C_1z + 2J_1) + \lambda_2(2F_2x + 2E_2y + 2C_2z + 2J_2)$$
$$\frac{\partial H}{\partial \lambda_1} = g_1(x, y, z) = 0 = \mathbf{p}^T Q_{sphere} \mathbf{p}$$
$$\frac{\partial H}{\partial \lambda_2} = g_2(x, y, z) = 0 = \mathbf{p}^T Q_{cone} \mathbf{p},$$

where $v_{i,x}, v_{i,y}, v_{i,z}$ are the components of the original velocity $\mathbf{v}_i$. This system of equations was solved numerically in Matlab using the fsolve command. The original velocity $\mathbf{v}_i$ was provided as the initial guess.

The intersection of two cones and the sphere of constant speed is two points. The closer of these points was found numerically using fsolve to find $\mathbf{v}_i' = [x\ y\ z]$ on the three constraint surfaces $\mathbf{g} = [g_1\ g_2\ g_3]^T = \mathbf{0}$. The computations were made more efficient by also providing fsolve with the Jacobian of the constraint equations

$$Jac(\mathbf{g}) \equiv \begin{bmatrix} \frac{\partial g_1}{\partial x} & \frac{\partial g_1}{\partial y} & \frac{\partial g_1}{\partial z} \\ \frac{\partial g_2}{\partial x} & \frac{\partial g_2}{\partial y} & \frac{\partial g_2}{\partial z} \\ \frac{\partial g_3}{\partial x} & \frac{\partial g_3}{\partial y} & \frac{\partial g_3}{\partial z} \end{bmatrix},$$

$$\text{where } \frac{\partial g_i}{\partial x} = 2A_i x + 2D_i y + 2F_i z + 2G_i$$
$$\frac{\partial g_i}{\partial y} = 2B_i y + 2D_i x + 2E_i z + 2H_i$$
$$\frac{\partial g_i}{\partial z} = 2C_i z + 2E_i y + 2F_i x + 2J_i.$$

3.2.2 Variable Speed

When the magnitude of the velocity is allowed to vary, the speed constraint becomes the solid circle or sphere of maximum velocity v_{max}. That is, $\mathbf{v}_i'$ lies within a closed two or three dimensional ball centered at the origin: $\mathbf{v}_i' \in B_2(v_{max})$ or $\mathbf{v}_i' \in B_3(v_{max})$ where $B_n(r) \equiv \{\mathbf{x} \in \mathbb{R}^n : \|\mathbf{x}\| \leq r\}$). Potential optima for this maneuver include locations at

1. the nearest point to $\mathbf{v}_i$ on a single collision cone in two and three dimensions,

2. the nearest point to $\mathbf{v}_i$ on the intersection of a collision cone and the spherical shell (circle) of maximum speed in three (two) dimensions,

3. the nearest point on (or simply the intersection of) two collision cones in three (two) dimensions, or

4. the intersection of two collision cones and the sphere of maximum speed in three dimensions.

Location 1: If there was only one potential obstacle and v_{max} was unbounded, the nearest point on the single collision cone would be the optimal solution, $\mathbf{v}_i^*$. In both two and three

dimensions, the nearest point on a cone is the orthogonal projection of $\mathbf{v}_i$ onto the cone surface

$$\mathbf{v}_i' = \mathbf{v}_j + (\hat{\mathbf{c}}^T \mathbf{v}_{ij})\hat{\mathbf{c}} \tag{3.3}$$

where $\hat{\mathbf{c}}$ is calculated as in (3.2). To understand why (3.3) holds for the three dimensional case, note that a line between $\mathbf{v}_i$ and $\mathbf{v}_i'$ must be normal to the cone surface. For the non-eccentric cones considered here, any plane through the cone axis is normal to the cone surface, and $\hat{\mathbf{c}}$ is constructed such that it lies in a plane with the cone axis and $\mathbf{v}_i$.

Location 2: If the first location does not satisfy the maximum velocity constraint, the closest feasible solution to $\mathbf{v}_i$ is on the surface of the cone with a magnitude of v_{max}. In two dimensions, this point is at

$$\mathbf{v}_i' = \mathbf{v}_j - b\hat{\mathbf{c}}, \qquad b = (\hat{\mathbf{c}}^T \mathbf{v}_j) \pm \sqrt{(\hat{\mathbf{c}}^T \mathbf{v}_j)^2 - \mathbf{v}_j^T \mathbf{v}_j + v_{max}^2}.$$

In three dimensions, the point can be calculated numerically using the Lagrange multipliers described in the previous section.

Location 3: If there are multiple cones present, it is possible that the optimal single-cone solutions (found at location 1 or 2) fall within another cone and are thus unsafe. Then the nearest safe point to $\mathbf{v}_i$ is at their intersection. In two dimensions, each cone edge is represented by a line and this intersection is simply a set of linear equations for each pair of edges. If an intersection point is outside the circle of v_{max}, it is dropped and only the intersection at the other edge is used (at least one edge of the cone must lie within v_{max} or it would not be causing a conflict with $\mathbf{v}_i$). In three dimensions, the point can be calculated numerically using the Lagrange multipliers described in the previous section by replacing the spherical surface constraint with a constraint representing the second cone.

Location 4: If the nearest point on the intersection of two cones is outside of the sphere of maximum velocity, then the final potential optimal location is the intersection of those cones and the sphere of maximum velocity which can be found using the method for three constraint surfaces presented in the previous section.

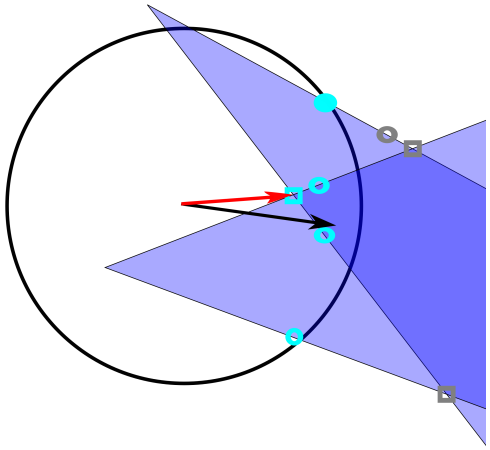

Figure 3.5: Depiction of the 2D variable speed maneuver. Possible optima for a single cone, at locations 1 and 2 (open and closed circles), and multiple cones, at location 3 (square), are shown for both feasible (cyan) and infeasible ($\|\mathbf{v}_i'\| > v_{max}$) (gray) points.

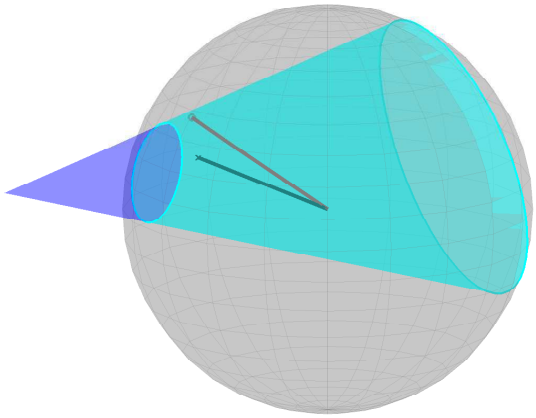

Figure 3.6: Depiction of the 3D variable speed maneuver. Potential velocities (cyan) are on the collision cone on or within the sphere .

Figures 3.5-3.6: The two- and three-dimensional variable speed maneuvers find optimal safe velocities (red) nearest to the original velocity (black) within the circle (black) or sphere (gray) of maximum speed.

3.2.3 Coordinate Systems

The original trajectory data for all of the species is provided in the global coordinate system, with the x_g-y_g plane coincident with the ground and z_g parallel or anti-parallel to gravity, shown in Figure 3.7. Body-fixed coordinates are calculated by rotating the global coordinates to align the x_b axis with the velocity of the animal and the y_b axis parallel to the ground; z_b is calculated as orthogonal to x_b and y_b. The transformation from global to body-fixed was done by calculating the pitch θ (angle about y_b) and yaw ψ (heading angle, about z_g) from the components of the velocity vector $\mathbf{v}_i$ as

$$\theta = \tan\left(\frac{v_{i,z}^2}{\sqrt{v_{i,x}^2 + v_{i,y}^2}}\right), \qquad \psi = \tan\left(\frac{v_{i,y}}{v_{i,x}}\right)$$

and then generating the Euler rotation matrix $\mathbf{R} = \mathbf{R}_x\mathbf{R}_y\mathbf{R}_z$ where

$$\mathbf{R}_x = \begin{bmatrix} 1 & 0 & 0 \\ 0 & \cos(\phi) & \sin(\phi) \\ 0 & -\sin(\phi) & \cos(\phi) \end{bmatrix}, \mathbf{R}_y = \begin{bmatrix} \cos(\theta) & 0 & -\sin(\theta) \\ 0 & 1 & 0 \\ \sin(\theta) & 0 & \cos(\theta) \end{bmatrix}, \mathbf{R}_z = \begin{bmatrix} \cos(\psi) & \sin(\psi) & 0 \\ -\sin(\psi) & \cos(\psi) & 0 \\ 0 & 0 & 1 \end{bmatrix}.$$

The roll angle ϕ is not available from the trajectory data, so it cannot be used to specify the body coordinates, so $\mathbf{R}_x = I_{3\times3}$. A rotation matrix is calculated for each frame based on the velocity of the focus $\mathbf{v}_i$ in that frame, then applied to the velocities and positions of all other objects j in the frame to obtain $\mathbf{r}_{b,j} = \mathbf{R}_i\mathbf{r}_j$ and $\mathbf{v}_{b,j} = \mathbf{R}_i\mathbf{v}_j$.

In both coordinate systems, the two-dimensional projection is obtained by setting the vertical components (along z_b or z_g) to zero. Information is lost in applying the projection, however the conflict detection is performed prior to flattening the data, ensuring only legitimate conflicts are included in the calculations.

3.3 Modeling Static Obstacles

To fully describe the scenes associated with each of the trajectories, the static objects need to be represented as static obstacles (with zero velocity). Other approaches to modeling static objects for collision avoidance algorithms based in velocity space include using truncated collision cones, which consider only collisions that would occur within a finite time span

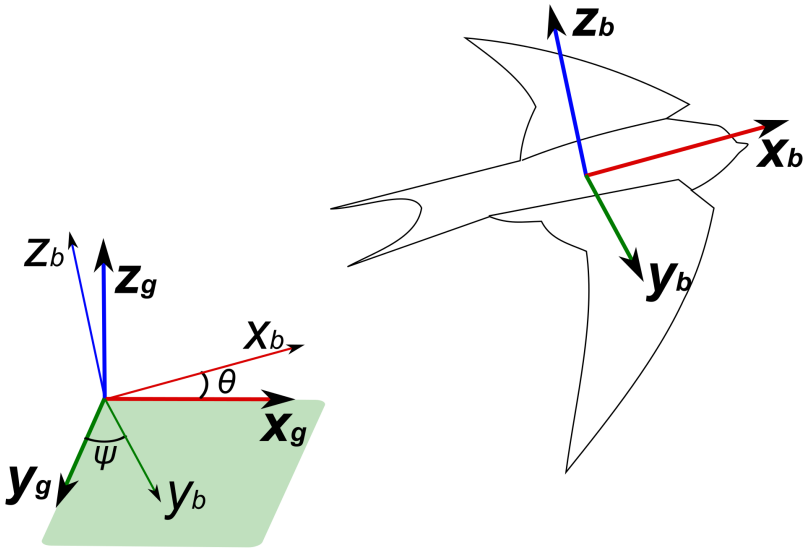

Figure 3.7: Depiction of the global (subscript g) and body fixed (subscript b) coordinate systems. In the body fixed coordinate system, the x_b axis is aligned with the velocity, y_b is parallel to the ground (defined by the $x_g - y_g$ plane), and z_b is defined as orthogonal to x_b and y_b.

[20] or using general quadric surfaces [36]. To utilize the DRCA algorithm, instead, static obstacles were sized and placed strategically so that the infinite look ahead and spherical shape could be maintained. Some static objects, such as silos, fit fairly neatly into the virtual circular barriers defined by d_{sep} with only a few static obstacles. Other objects, such as long roof lines or walls of a fish tank, require more care to ensure that they do not create many potential conflicts or completely occlude travel in a given direction.

3.3.1 Cylindrical Objects

Objects that prevented animals from occupying a cylindrical volume with a low height to radius ratio were modeled as a constant stack of static obstacles. The obstacles are placed along the center line of the cylindrical object and spaced to encompass the object with some small amount of overshoot, d_o. The spacing c is calculated based on the radius of the object

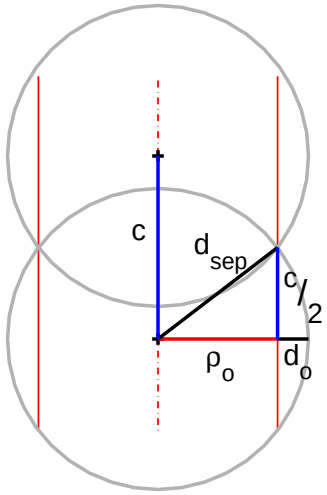

Figure 3.8: Geometry of static obstacles for a cylindrical object. The spacing c (blue) of the static obstacles (black +) is determined so the static object (red dashed centerline, solid extents) of radius ρ_0 (red) will be completely encompassed by the obstacles (gray circles) generated by $d_{sep} = \rho_0 + d_0$.

ρ_o and a maximum separation excess d_o through simple geometry

$$c = 2\sqrt{d_{sep,cyl}^2 - \rho_0^2}$$

where $d_{sep,cyl} = \rho_0 + d_0$ (Figure 3.8). The overshoot was set to be $d_0 = d_{sep,species}$. The silos of the static flock scene are shown with the modeled obstacles in Figure 3.9.

3.3.2 Long, Thin Objects

Objects with a high height to radius ratio could be modeled as cylinders, but that choice would introduce many new objects to the conflict checking calculations which would be computationally expensive. Instead, obstacles were placed individually for each focus using the position and direction of travel of the focus. The location of an adaptive obstacle was chosen by offsetting the nearest place on the line defining the edge of the object by an angle

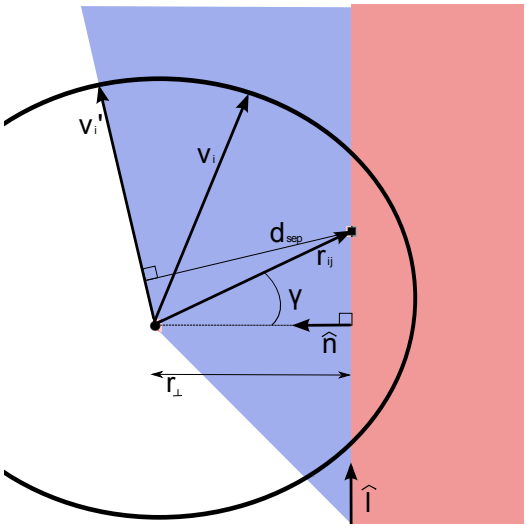

Figure 3.9: Geometry for placing a static obstacle (black dot) to prevent collision with a long, thin object such as the eaves of a building (red). Potential velocity and directions that would be covered by the constant speed collision cone (blue area) are included for reference.

γ, as depicted in Figure 3.9. This method is based on the idea that an animal may travel parallel to an object by keeping it at a fixed distance through peripheral vision cues.

To place the objects, unit vectors along and normal to the object, $\hat{\mathbf{l}}$ and $\hat{\mathbf{n}}$ respectively, were calculated as

$$\hat{\mathbf{l}} = \frac{\mathbf{x}_2 - \mathbf{x}_1}{\|\mathbf{x}_2 - \mathbf{x}_1\|}, \qquad \hat{\mathbf{n}} = \hat{\mathbf{l}} \times \hat{\mathbf{k}}$$

where $\mathbf{x}_1$ and $\mathbf{x}_2$ are points on the object, and $\hat{\mathbf{k}}$ is a unit vector chosen based on the geometry. For the eaves of a building which are parallel to the ground, $\hat{\mathbf{k}} = \begin{bmatrix} 0 & 0 & 1 \end{bmatrix}$ was used so the component of distance perpendicular to the wall in the horizontal direction (parallel to the ground) could be computed as

$$r_\perp = (\mathbf{x}_0 - \mathbf{r}_i) \cdot \hat{\mathbf{n}}.$$

The perpendicular distance was used to scale the component along the wall $r_\parallel$ to offset the object by an angle γ along the wall

$$r_\parallel = r_\perp \tan(\gamma).$$

Combining these components with the vertical offset $r_z = \mathbf{r}_{i,z} - \mathbf{x}_{0,z}$ gives the relative

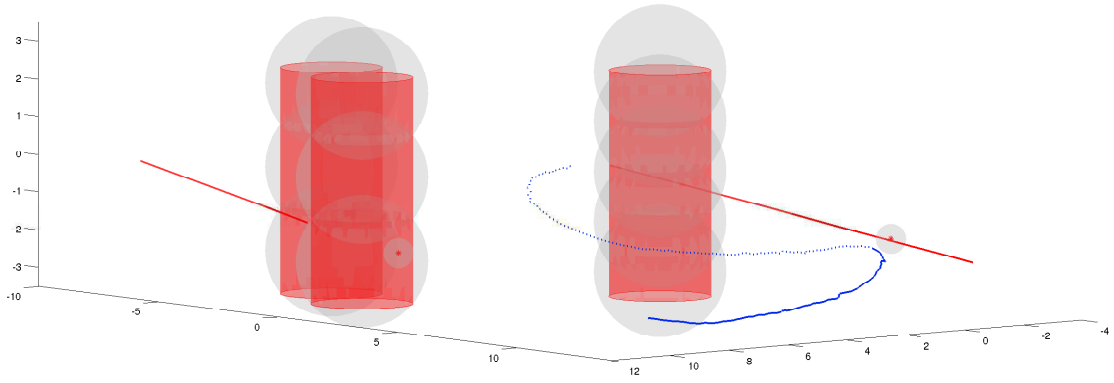

Figure 3.10: Trajectory of a single swallow (blue, previous trajectory is solid) with static obstacles (red) and their modeled occluded volumes (gray spheres). The silos are constant and the adaptive static obstacles on the eaves (centered at red *) are calculated for the plotted trajectory.

location $\mathbf{r}_{ij}$ of the obstacle to the focus animal. The absolute position of the static obstacle is obtained by adding the relative position to the position of the focus animal $\mathbf{r}_i$

$$\mathbf{r}_j = \underbrace{r_{\parallel}\hat{\mathbf{l}} - r_{\perp}\hat{\mathbf{n}} + r_z\hat{\mathbf{k}}}_{\mathbf{r}_{ij}} + \mathbf{r}_i.$$

The separation distance for the static obstacle was chosen to be the same as for the animal $d_{sep,line} = d_{sep,species}$. The eaves in the static flock scene are shown with the modeled obstacles for one animal in Figure 3.9.

3.3.3 Planes

In position space, it would be logical to model the walls of a fish tank by placing an obstacle far behind the wall and with a large required separation distance, which would approximate a flat obstacle near the wall. When done this way in velocity space, that method would create a cone that was nearly a half-space, effectively preventing the fish from ever turning in the direction of that wall. To avoid this effect, the velocity vector was projected onto each wall (including the bottom of the tank) creating line objects that could be approached using the technique from the previous section. The walls were aligned with the global coordinate

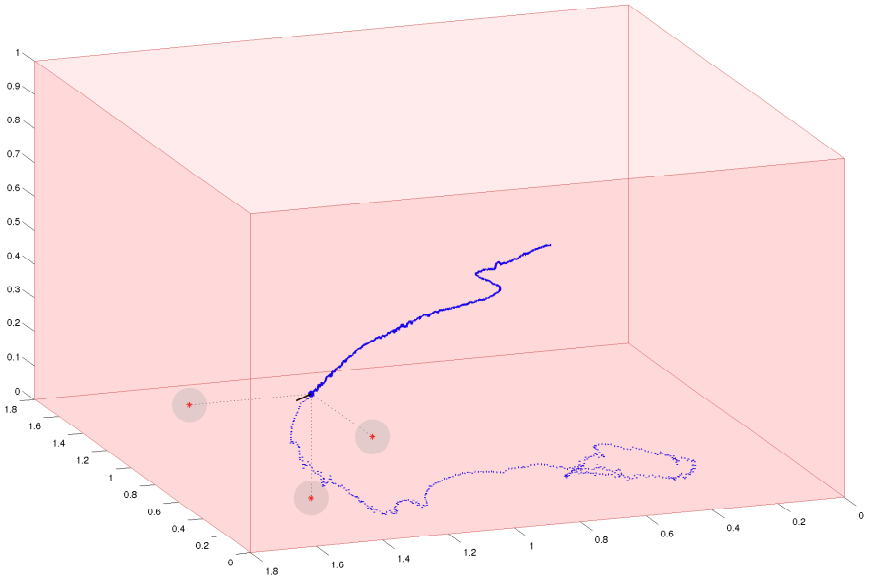

Figure 3.11: Trajectory of a single fish (blue, previous trajectory is solid) with static obstacles on the walls (red *) surrounded by their separation distance (gray spheres). Shown with $\alpha = 0$.

system, so the projection was done by setting the x or y component zero or 1.8 for side walls or setting the z component to zero for the bottom. The adaptive obstacles were only generated in the direction of travel unless the focus was close to the wall; for the fish, walls were modeled whenever the focus was within 4 body lengths of the wall (Figure 3.11).

Chapter 4

ANALYSIS

The optimal velocity for each variation of the DRCA algorithm was calculated from the position and velocity data all of in the three-dimensional trajectories, indicating what an engineered system running the algorithm would do if it were face with the same situation. The difference between observed and algorithmically optimal velocities was computed and used to find correlation rates for each of the DRCA algorithms and a range of sensing parameters.

4.1 DRCA with Trajectory Data

To generate the basis for comparison with the trajectory data, each animal was considered as the focus (agent i) with the other animals within the sensing range considered as dynamic obstacles. For each frame in which the focus animal was present, conflicts were checked for the positions and velocities of the other animals within the sensing distance as well as for the positions of static obstacles. The sensing distance was determined by a combination of metric and topological distances, so only the nearest N animals within d_a of the focus were considered. If a conflict was present, each of the six deconfliction maneuvers - constant and variable speed in three dimensions and two dimensions with each coordinate system - was used to calculate an optimal velocity $\mathbf{v}_i^*$. If animals were already in a collision, the frame was excluded from consideration. Also, to exclude swallows perching on the barns, the DRCA was not applied to frames where their velocity was less than 3 meters per second.

The algorithmic parameters d_{sep}, v_c, and v_{max} were determined based on the biological characteristics of each species. The minimum required separation distance for each of the flying species was half of the wingspan, $d_{sep,bats} = 0.15$ and $d_{sep,swallows} = 0.2$ meters, and was a body length for the fish, $d_{sep,fish} = 0.05$ meters. The constant speed requirement, which would be prescribed in an engineered system, was calculated as the magnitude of

the focus animal's current velocity in each frame $v_c = \|\mathbf{v}_i\|$. The speed for the maximum velocity requirement was set higher than the typical cruising speed found in the literature for the bats and swallows, at 11 and 18 meters per second, and based on the maximum used in models of fish behavior set at 0.6 meters per second (12 body lengths per second [2]).

4.2 Comparison Metric

For every conflict, each DRCA optimal velocity $\mathbf{v}_i^*$ was compared to the observed velocity $\mathbf{v}_i^o$ in a subsequent frame. The comparison was done using the velocity observed in the next frame (immediately subsequent to the one used for DRCA calculations) as well as the velocity required to get to the focus animal's position at its reaction time, with the expectation that the results would improve for the reaction time. The reaction time was considered as 50 milliseconds for all species per the recommendation of biologists familiar with the species. The metric used was the normed difference between the velocity vectors in three-dimensions: $\Delta v = ||\mathbf{v}_i^* - \mathbf{v}_i^o||$. A normalized histogram of Δv values was generated for each focus animal with bins sized according to the standard deviation of the velocities for that species. Each histogram was normalized by the total number of conflicts experienced by the focus. The level of correlation is defined here as the portion of conflict resolutions falling into the first bin of the normalized histogram. The subsequent plots show the level of correlation averaged over all focus animals within a species that experienced conflict for each data point (i.e. each maneuver, d_a, and number of influential neighbors).

4.3 Results

The results of the analysis indicate that the optimal velocity prescribed by the different versions DRCA algorithm correlates relatively well with the available trajectory data at the reaction time. However, there are some interesting differences between the results of the different species.

4.3.1 Bats

The correlation for bats is high for all of the deconfliction maneuvers and almost all sensing parameters. The reaction time is consistently better correlated than the next frame data.

Comparing Figures 4.1-4.6, the number of nearest neighbors does not appear to be a large factor in the agreement levels; the correlation is slightly higher for $N = 3$, but well within the error bounds. Shown in Figures 4.7-4.12, changing the radius of attraction appears to have more of an impact, with lower correlation for all maneuvers with $d_a = 0.5$ meters and highest, albeit not by much, for $d_a = 3$ meters.

4.3.2 Swallows

The correlation of the swallow data is relatively high, however the next frame data is unexpectedly better correlated than the reaction time data, except for a single data point. A definitive reason for the reduced correlation at the reaction time was not found, however it could be due to preemptive reactions (the swallow recognizes and avoids a conflict before the algorithm), collision avoidance being a low priority (compared to chasing other swallows, foraging, landing, etc.), data artifacts, or some combination thereof. It was originally thought that wing beat fluctuations may be a large factor, however the relative correlation did not change when wingbeat oscillations were filtered out of the trajectory data. The correlation for swallows is highest for the three-dimensional maneuvers, and lowest for the two-dimensional maneuver using global coordinates. The number of nearest neighbors has relatively little effect, although the correlation slightly increases with N for the two-dimensional cases (Figures 4.13-4.18). In the three-dimensional and two-dimensional body-fixed cases, the radius of attraction is best correlated for $d_a = 1.5$ meters and otherwise fairly constant (see Figures 4.13-4.18). In the two-dimensional global coodrinates the value is relatively constant, except slightly lower for $d_a = 3$ meters.

4.3.3 Fish

The fish data shows the largest improvement in correlation between the two- and three-dimensional maneuvers and also between the next frame and reaction frame data. The difference is most pronounced for the all untrained fish data, shown in Figures 4.25-4.30 for a range of N and 4.37-4.42 for a range of d_a, in which the level of correlation at the reaction time increases from two-dimensional global to body coordinates and again from

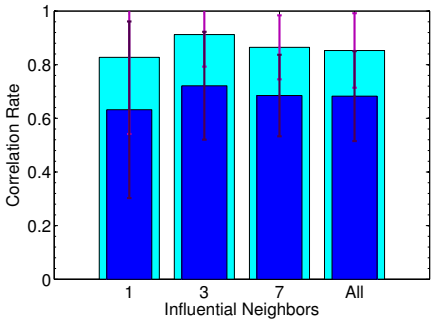

Figure 4.1: Bats Nearest Neighbors 2D Constant Speed, Global Coordinates

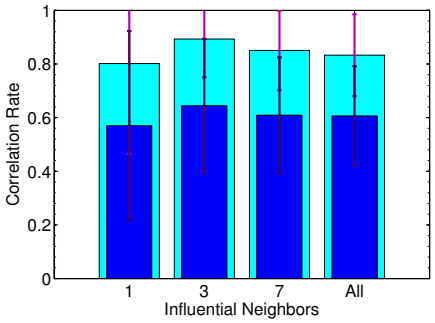

Figure 4.2: Bats Nearest Neighbors 2D Constant Speed, Body-Fixed Coordinates

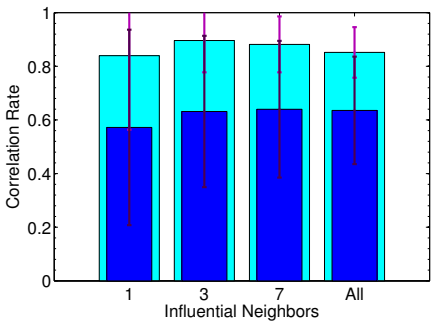

Figure 4.3: Bats Nearest Neighbors 3D Constant Speed

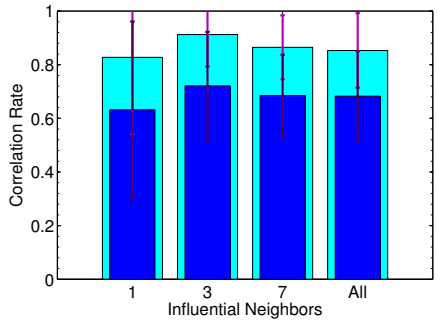

Figure 4.4: Bats Nearest Neighbors 2D Variable Speed, Global Coordinates

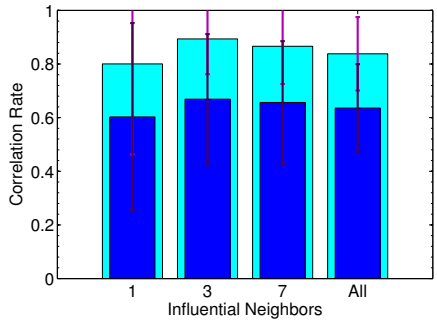

Figure 4.5: Bats Nearest Neighbors 2D Variable Speed, Body-Fixed Coordinates

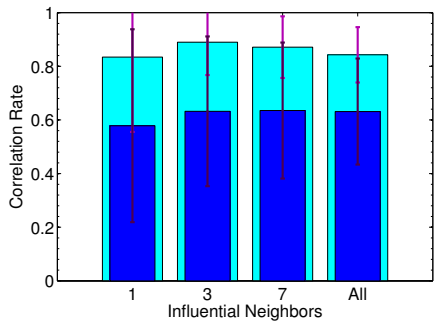

Figure 4.6: Bats Nearest Neighbors 3D Variable Speed

Figures 4.1-4.6: Correlation corresponding to range of influential nearest neighbors for $\mathbf{v}_i^o$ in the next frame (cyan) and at the reaction time (blue) in two and three-dimensions with $d_a = \infty$ for bats.

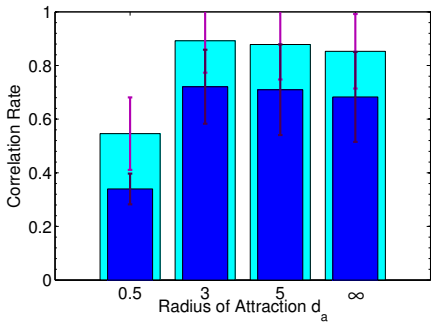

Figure 4.7: Bats Metric Sensing Range 2D Constant Speed, Global Coordinates

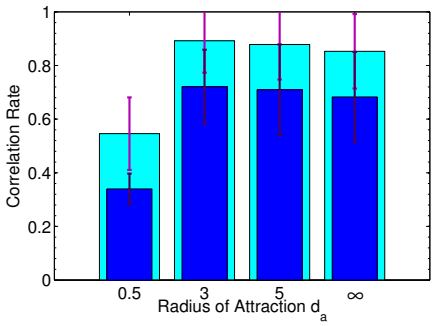

Figure 4.10: Bats Metric Sensing Range 2D Variable Speed, Global Coordinates

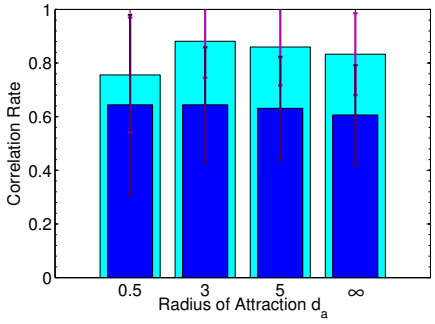

Figure 4.8: Bats Metric Sensing Range 2D Constant Speed, Body-Fixed Coordinates

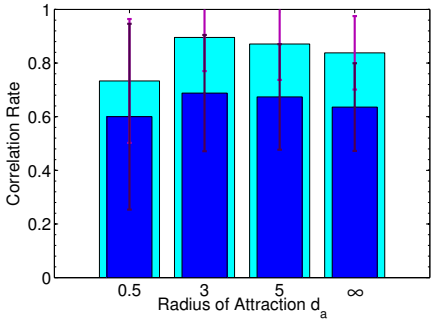

Figure 4.11: Bats Metric Sensing Range 2D Variable Speed, Body-Fixed Coordinates

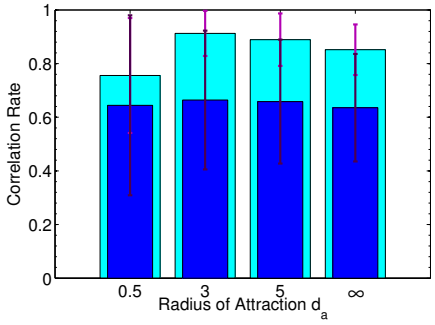

Figure 4.9: Bats Metric Sensing Range 3D Constant Speed

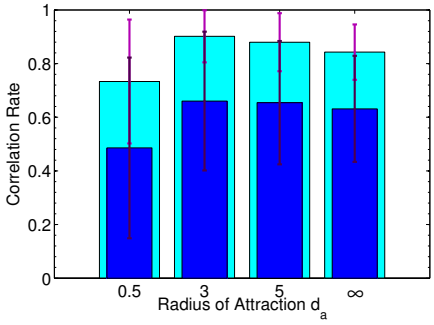

Figure 4.12: Bats Metric Sensing Range 3D Variable Speed

Figures 4.7-4.12: Correlation corresponding to range of radius of attraction for $\mathbf{v}_i^o$ in the next frame (cyan) and at the reaction time (blue) in two and three-dimensions with $N =$ all for bats.

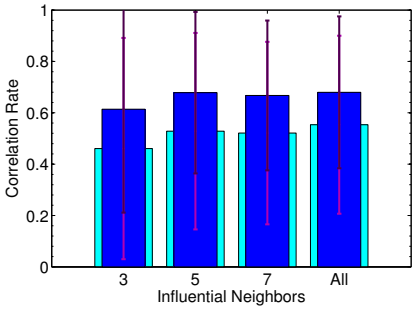

Figure 4.13: Swallows Nearest Neighbors 2D Constant Speed, Global Coordinates

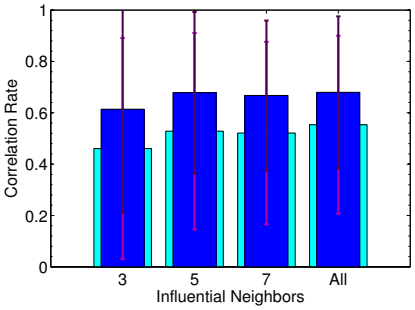

Figure 4.16: Swallows Nearest Neighbors 2D Variable Speed, Global Coordinates

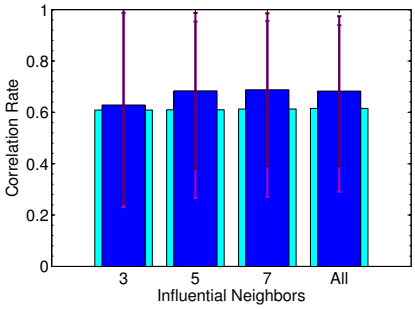

Figure 4.14: Swallows Nearest Neighbors 2D Constant Speed, Body-Fixed Coordinates

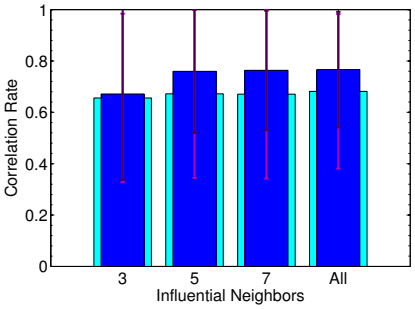

Figure 4.17: Swallows Nearest Neighbors 2D Variable Speed, Body-Fixed Coordinates

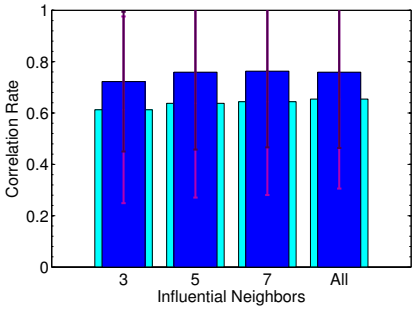

Figure 4.15: Swallows Nearest Neighbors 3D Constant Speed

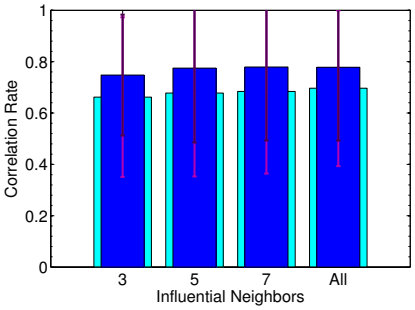

Figure 4.18: Swallows Nearest Neighbors 3D Variable Speed

Figures 4.13-4.18: Correlation corresponding to range of influential nearest neighbors for $\mathbf{v}_i^o$ in the next frame (cyan) and at the reaction time (blue) in two and three-dimensions with $d_a = \infty$ for swallows.

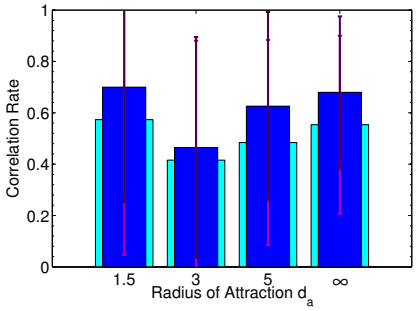

Figure 4.19: Swallows Metric Sensing Range 2D Constant Speed, Global Coordinates

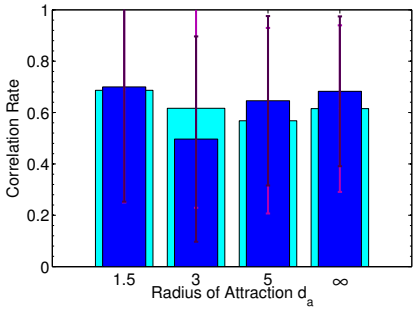

Figure 4.20: Swallows Metric Sensing Range 2D Constant Speed, Body-Fixed Coordinates

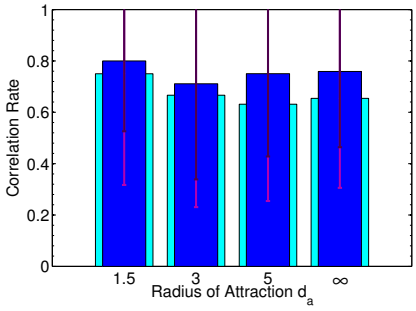

Figure 4.21: Swallows Metric Sensing Range 3D Constant Speed

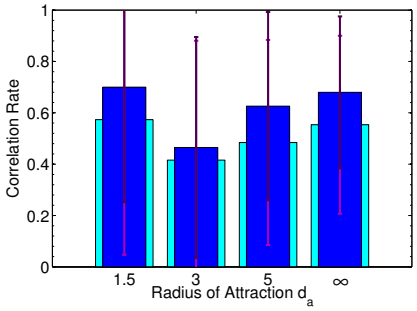

Figure 4.22: Swallows Metric Sensing Range 2D Variable Speed, Global Coordinates

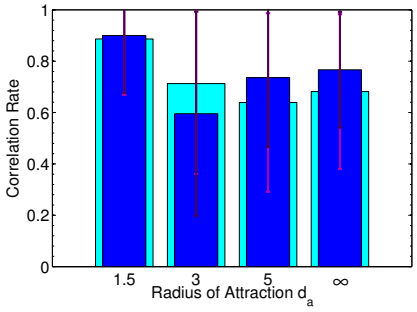

Figure 4.23: Swallows Metric Sensing Range 2D Variable Speed, Body-Fixed Coordinates

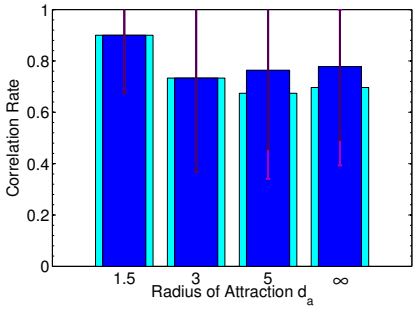

Figure 4.24: Swallows Metric Sensing Range 3D Variable Speed

Figures 4.19-4.24: Correlation corresponding to range of radius of attraction for $\mathbf{v}_i^o$ in the next frame (cyan) and at the reaction time (blue) in two and three-dimensions with $N =$ all for swallows.

body coordinates to three dimensions. The trained fish data in Figures 4.31-4.36 for a range of N and 4.43-4.48 for a range of d_a shows similar levels of correlation for both of the two-dimensional maneuvers and higher correlation for the three-dimensional case. Similar levels of correlation are observed over the range of nearest neighbors considered, with slightly opposite trends between the data sets: the correlation decreases with increasing N for the untrained fish, but increases with increasing N for the trained fish. The range of attraction does not affect the correlation rate for the untrained fish, but the correlation increases with increasing d_a for the trained fish. This result is likely due to the lower density of the trained fish, since increasing d_a increases the number of fish considered more dramatically for the trained than it does with the untrained fish.

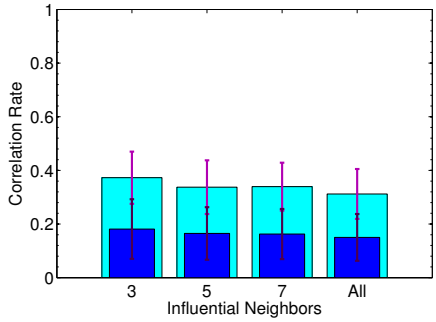

Figure 4.25: Untrained Fish Nearest Neighbors 2D Constant Speed, Global Coordinates

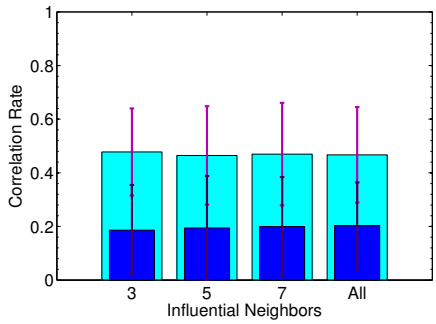

Figure 4.26: Untrained Fish Nearest Neighbors 2D Constant Speed, Body-Fixed Coordinates

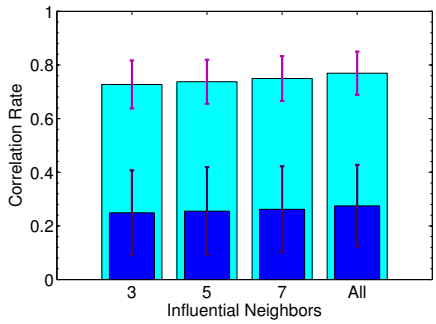

Figure 4.27: Untrained Fish Nearest Neighbors 3D Constant Speed

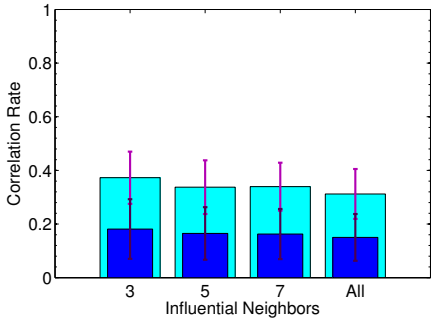

Figure 4.28: Untrained Fish Nearest Neighbors 2D Variable Speed, Global Coordinates

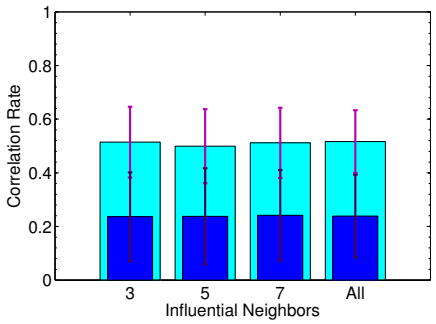

Figure 4.29: Untrained Fish Nearest Neighbors 2D Variable Speed, Body-Fixed Coordinates

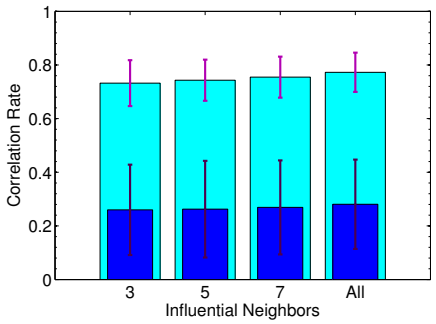

Figure 4.30: Untrained Fish Nearest Neighbors 3D Variable Speed

Figures 4.25-4.30: Correlation corresponding to range of influential nearest neighbors for $\mathbf{v}_i^o$ in the next frame (cyan) and at the reaction time (blue) in two and three-dimensions with $d_a = \infty$ for fish in the 0-15 (all untrained) data set.

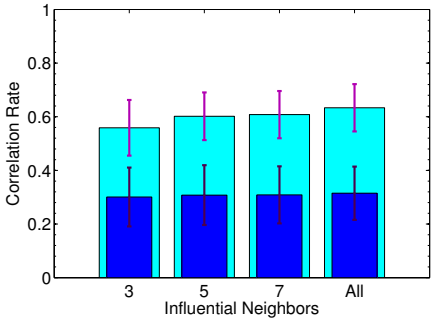

Figure 4.31: Trained Fish Nearest Neighbors 2D Constant Speed, Global Coordinates

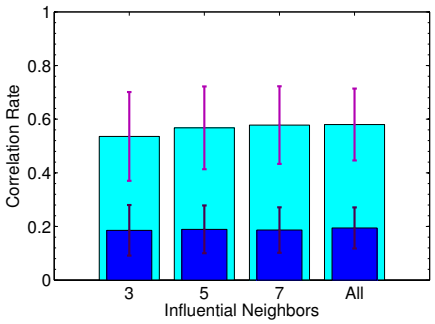

Figure 4.32: Trained Fish Nearest Neighbors 2D Constant Speed, Body-Fixed Coordinates

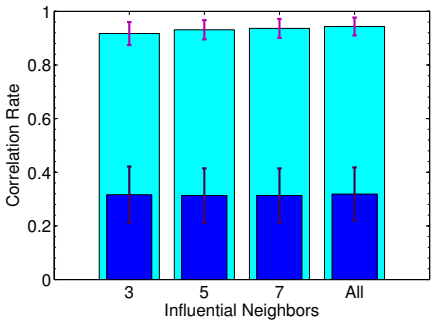

Figure 4.33: Trained Fish Nearest Neighbors 3D Constant Speed

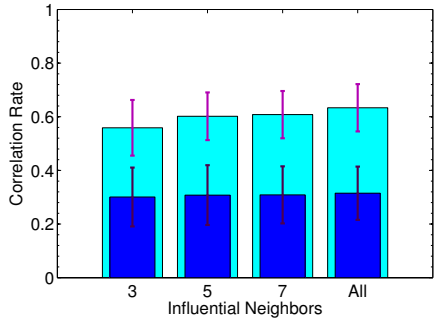

Figure 4.34: Trained Fish Nearest Neighbors 2D Variable Speed, Global Coordinates

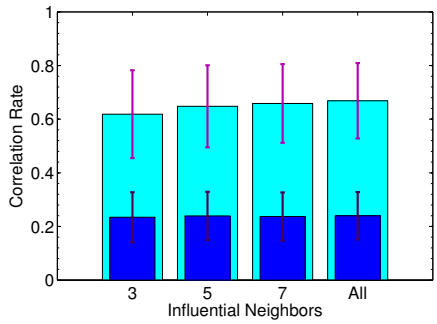

Figure 4.35: Trained Fish Nearest Neighbors 2D Variable Speed, Body-Fixed Coordinates

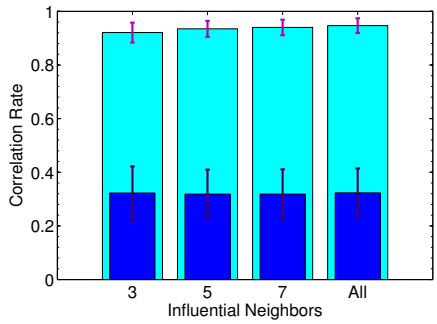

Figure 4.36: Trained Fish Nearest Neighbors 3D Variable Speed

Figures 4.31-4.36: Correlation corresponding to range of influential nearest neighbors for $\mathbf{v}_i^o$ in the next frame (cyan) and at the reaction time (blue) in two and three-dimensions with $d_a = \infty$ for fish in the 15-0 (all trained) data set.

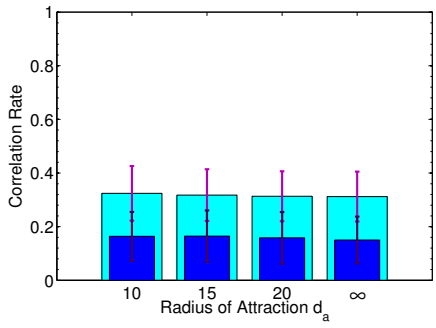

Figure 4.37: Untrained Fish Metric Sensing Range 2D Constant Speed, Global Coordinates

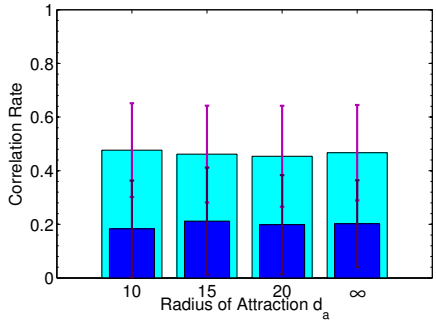

Figure 4.38: Untrained Fish Metric Sensing Range 2D Constant Speed, Body-Fixed Coordinates

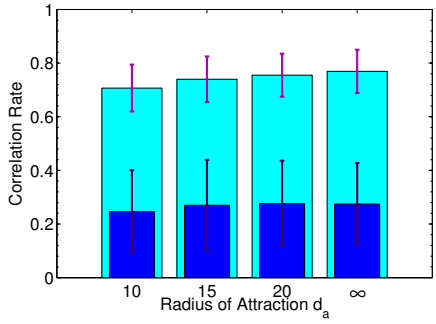

Figure 4.39: Untrained Fish Metric Sensing Range 3D Constant Speed

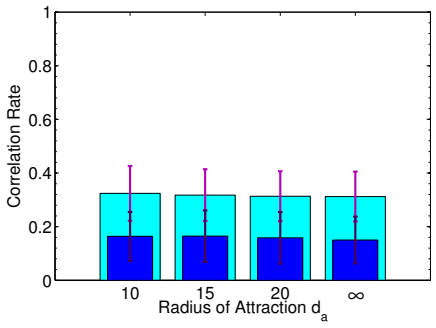

Figure 4.40: Untrained Fish Metric Sensing Range 2D Variable Speed, Global Coordinates

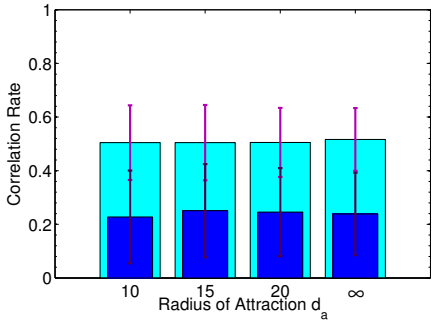

Figure 4.41: Untrained Fish Metric Sensing Range 2D Variable Speed, Body-Fixed Coordinates

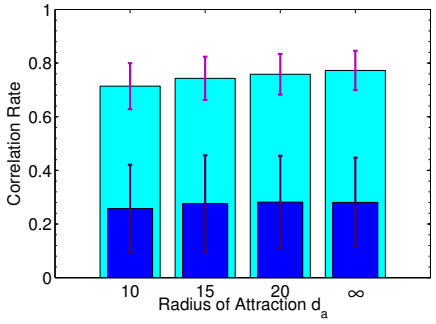

Figure 4.42: Untrained Fish Metric Sensing Range 3D Variable Speed

Figures 4.37-4.42: Correlation corresponding to range of radius of attraction for $\mathbf{v}_i^o$ in the next frame (cyan) and at the reaction time (blue) in two and three-dimensions with $N = all$ for fish in the 0-15 (all untrained) data set.

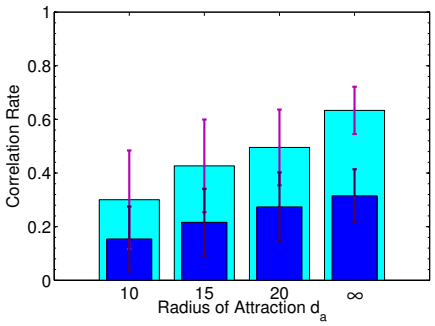

Figure 4.43: Trained Fish Metric Sensing Range 2D Constant Speed, Global Coordinates

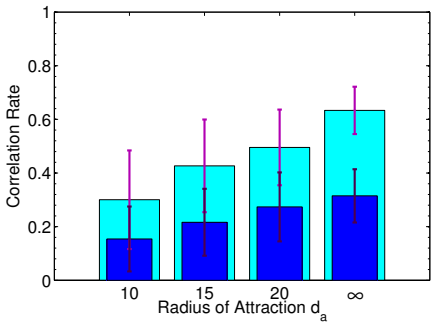

Figure 4.46: Trained Fish Metric Sensing Range 2D Variable Speed, Global Coordinates

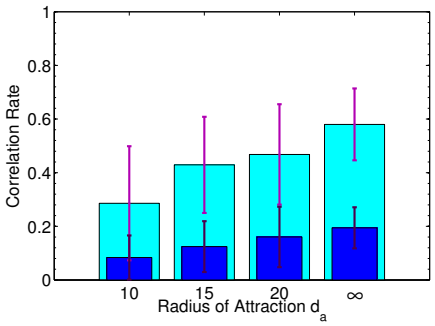

Figure 4.44: Trained Fish Metric Sensing Range 2D Constant Speed, Body-Fixed Coordinates

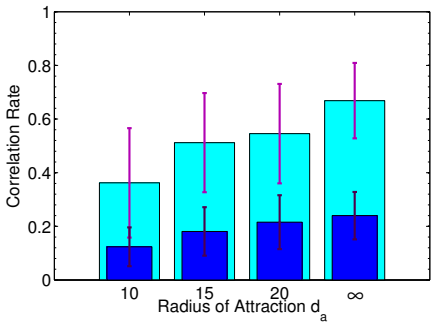

Figure 4.47: Trained Fish Metric Sensing Range 2D Variable Speed, Body-Fixed Coordinates

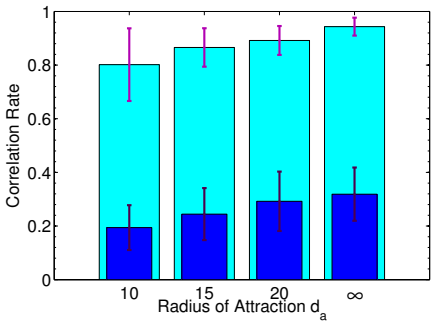

Figure 4.45: Trained Fish Metric Sensing Range 3D Constant Speed

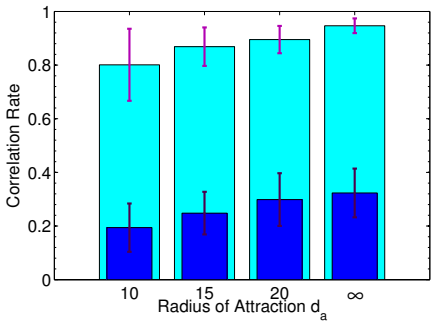

Figure 4.48: Trained Fish Metric Sensing Range 3D Variable Speed

Figures 4.43-4.48: Correlation corresponding to range of radius of attraction for $\mathbf{v}_i^o$ in the next frame (cyan) and at the reaction time (blue) in two and three-dimensions with $N = all$ for fish in the 15-0 (all trained) data set.

4.3.4 Species Comparison

Condensed plots for a single data point show the correlation for all of the species under consideration in Figures 4.49-4.54. The data was collected for $N = 7$ influential neighbors for all species and a metric sensing range of $d_a = 5$ meters for both flying species and $d_a = 0.2$ meters for the fish. In terms of next frame versus reaction time results, the fish and bats behave similarly - with some correlation in the next frame but much higher correlation at their reaction time; the swallows show the opposite. The flying species behave relatively similarly in all three maneuvers, which is consistent with a preference of changes in heading to altitude. The fish appear to utilize the third dimension more, showing higher correlation for the three dimensional maneuver. The energy cost for the fish to change their height is lower than the flying species, so it seems reasonable the flying species would be less likely to change their vertical position.

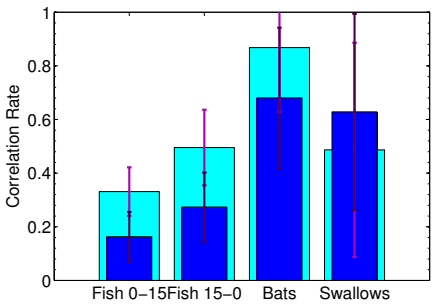

Figure 4.49: Species Comparison for 2D Constant Speed, Global Coordinates

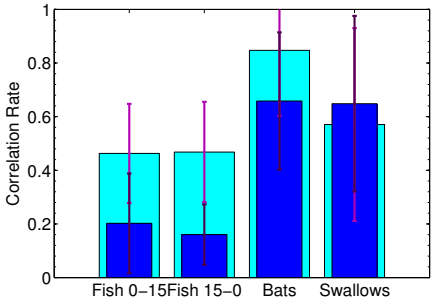

Figure 4.50: Species Comparison for 2D Constant Speed, Body-Fixed Coordinates

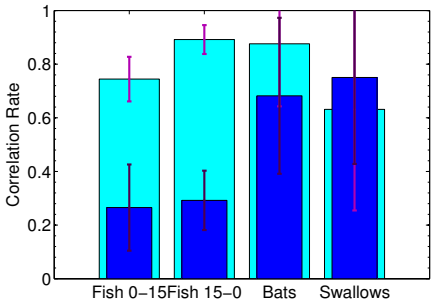

Figure 4.51: Species Comparison for 3D Constant Speed

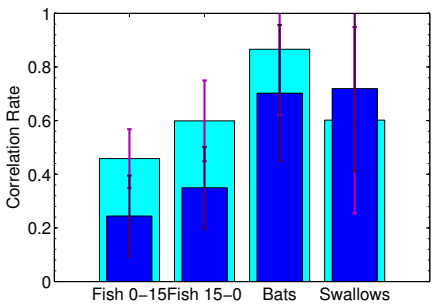

Figure 4.52: Species Comparison for 2D Variable Speed, Global Coordinates

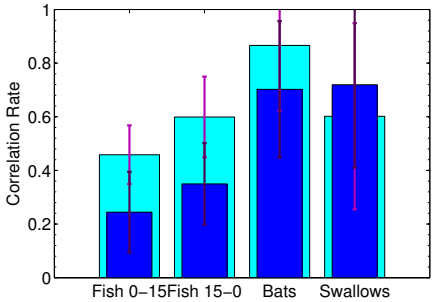

Figure 4.53: Species Comparison for 2D Variable Speed, Body-Fixed Coordinates

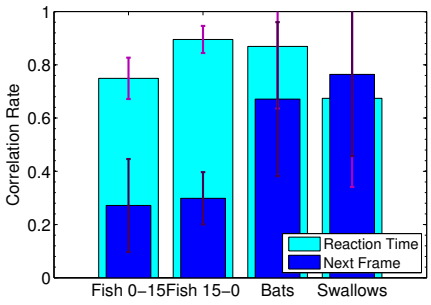

Figure 4.54: Species Comparison for 3D Variable Speed

Figures 4.49-4.54: Comparison of correlation between species with 7 influential nearest neighbors and $d_a = 0.2$ meters for fish and $d_a = 5$ meters for bats and swallows.

4.4 Additional Comparisons & Metrics

In addition to comparisons with the DRCA algorithm, other metrics were also considered to try to better understand the interactions observed in trajectory data captured by the comparison presented above. Specifically, the discrepancy between the swallows and other species with respect to behavior at the reaction time. A subset of those methods is presented here, including a comparison of social force to acceleration and a method of gauging a focus animal's response to another animal or static object coming within a specified distance.

4.4.1 Acceleration versus Social Force

The social force acting on a focus animal is the sum of the forces between it and the other animals. Repulsive or attractive forces act along the vector between each pair of animals $\hat{\mathbf{r}}_{ij}$ with a magnitude scaled by some function f of the distance between them

$$\mathbf{f}_{s,ij} = \sum_{j=1}^{N} \hat{\mathbf{r}}_{ij} f(\|\mathbf{r}_{ij}\|).$$

In models of social force in fish, the magnitude of $f(\|\mathbf{r}_{ij}\|)$ is negative for neighbors in the repulsive zone ($\|\mathbf{r}_{ij}\| < d_r$) and positive for those in the attractive zone ($d_{align} < \|\mathbf{r}_{ij}\| < d_a$) [37]; if alignment is being considered, there is instead an alignment force acting to match the headings for animals in the alignment zone ($d_r < \|\mathbf{r}_{ij}\| < d_{align}$), otherwise this is considered the neutral zone.

For the study here, the social force was calculated in body coordinates for each animal using a piecewise linear function. The observed accelerations were plotted against the social force, shown for birds and bats in Figures 4.55 - 4.58. One would expect to see a correlation between the social force and acceleration (similar to if a physical force were being applied), however that is not apparent in the data. Large accelerations happen when there is little social force and there is no apparent correlation between sign of social force and acceleration (i.e. a social force in the $-x$ direction does not induce a decrease in tangential velocity).

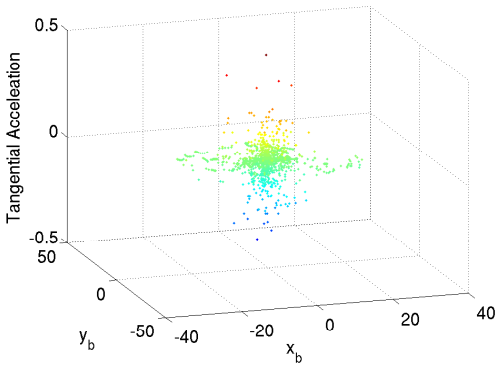

Figure 4.55: Tangential component of acceleration versus social foce in swallows.

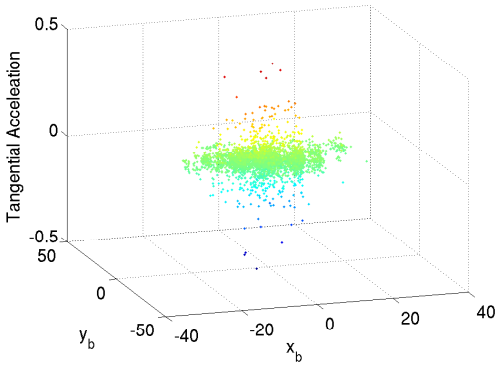

Figure 4.56: Tangential component of acceleration versus social foce in bats.

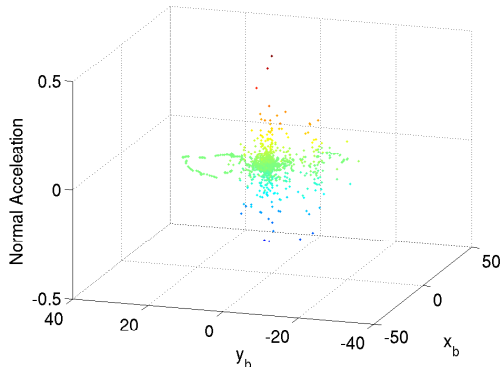

Figure 4.57: Normal component of acceleration versus social foce in swallows.

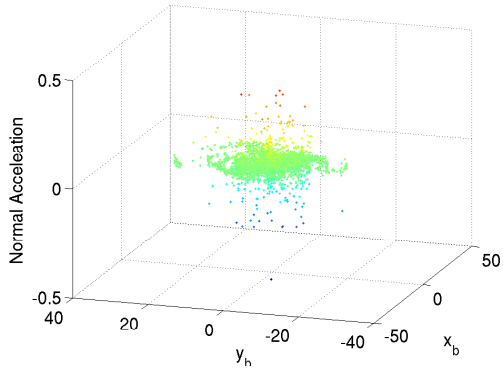

Figure 4.58: Normal component of acceleration versus social foce in bats.

Figures 4.55-4.58: The tangential and normal components of acceleration (vertical axis and colormap) of the swallow flock (top) and bat (bottom) trajectories plotted against the social force experienced in $x-y$ body coordinates. If the behavior was well modeled by the social force function, then a relation between tangential and normal acceleration and social force in x_b and y_b directions, respectively, should be apparent. The clustering of data points indicates the behavior is not well modeled.

4.4.2 Reaction Sphere

This analysis investigates the relationship between the introduction of nearby objects (other animals or static objects) into a sphere and changes in animal behavior. That is, the reaction to animals first entering within d_a rather than the prolonged interactions with animals within some d_a as was considered previously. The study was primarily focused on the behavior of swallows, and reaction sphere radii of 0.5 to 5 meters were considered. The reactions were quantified by the change in body fixed velocity and acceleration from a reaction time (50 milliseconds) before and after the other object entered the reaction sphere. For example, the magitude of acceleration changes in body fixed coordinates

$$||(v_{current,react^-} - v_{react^-,react^-}) - (v_{react^+,current} - v_{current,current})||_2,$$

where v_{f_1,f_2} indicates velocity in frame f_1 in body-fixed coordinates relative to frame f_2, $react^{\pm}$ indicates current frame $\pm$ reaction frames (5 for swallows: 50 msec reaction time for data collected at 100 Hz). The above data were plotted and overlaid with markers indicating the relative position (forward, backward, right, or left) and type (dynamic or static) of obstacles entering the reaction sphere (radius denoted by color), shown for a couple swallows in Figures 4.59-4.60. Objects entering the reaction spheres frequently coincided with local extrema of one or more components of the changing acceleration of velocity.

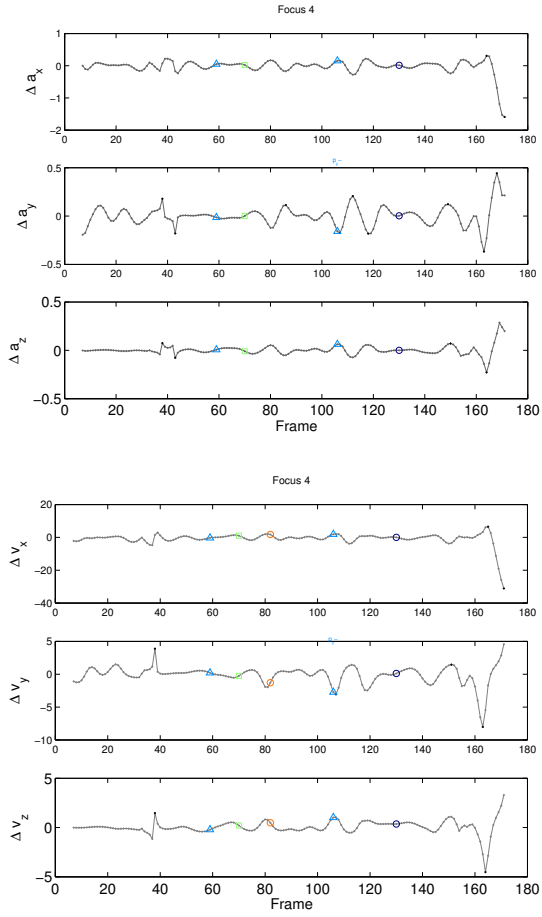

Figure 4.59: Reaction sphere data for focus animal 4

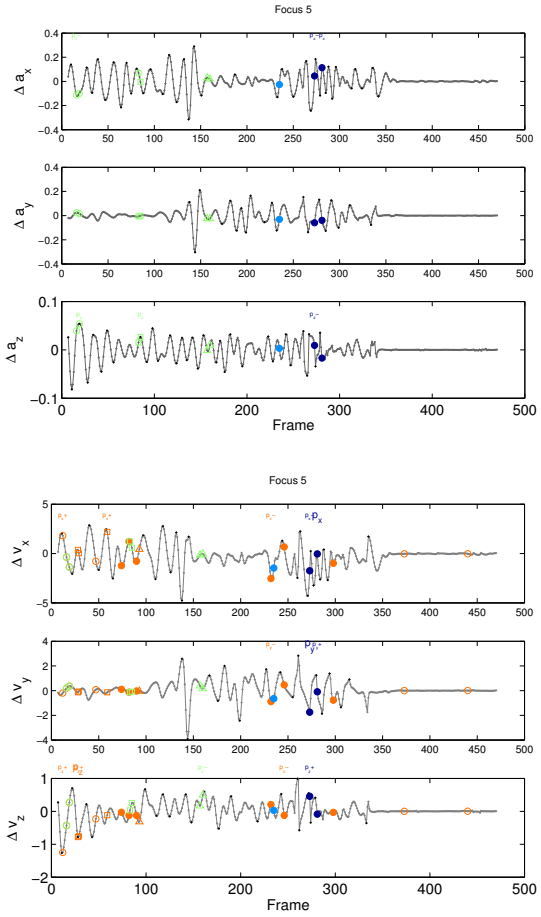

Figure 4.60: Reaction sphere data for focus animal 5

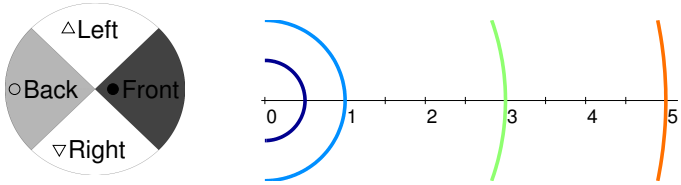

Figures 4.59-4.60: Reaction time plots showing the x_b, y_b, and z_b (subplots top to bottom) components of change in acceleration (top) and velocity (bottom) in for two swallows. The shape of the markers indicates if the obstacle is static (□) or the direction of the object and the color of the markers indicates the size of the reaction sphere (see key above).

Chapter 5

CONCLUSION AND FUTURE WORK

The collision avoidance behavior observed in biological species provides a good example for engineered systems. To this end, trajectory data gathered for three species, representing bats, birds, and fish, was compared to an engineered deconfliction algorithm. For each focus animal in each frame of data, conflict was checked by seeing if the focus's velocity fell within collision cones generated for each of the dynamic and static obstacles within sensing distance. If an eventual collision was detected, an optimal safe velocity was calculated by finding the velocity outside of all collision cones with the smallest deviation from the original velocity. The optimal velocity was calculated for four maneuvers: constant and variable speed in two and three dimensions. The original two-dimensional DRCA deconfliction maneuvers were extended to three dimensions to provide a more realistic comparison to the full three-dimensional perception and movement available to the swimming and flying species. The sensing distance was defined as the group of animals within a metric or topological distance of the focus animal; each of these distances was varied to assess its effect on the correlation of observed velocity to the algorithmic optimal velocity.

The comparison presented in this paper shows a reasonably high correlation between the engineered algorithm and observed biological trajectory data for the three-dimensional maneuvers at the reaction time. Calculating three-dimensional maneuvers increased the correlation for both constant and variable speed algorithms for all species. The reaction time analysis showed more agreement than next frame data for both the fish and bats, however the swallows did not follow that expected trend; this discrepancy has yet to be explained and could be the subject of further study. Neither metric nor topological sensing distance showed a clear relationship with the correlation rate, however there were some trends over the metric sensing distance. Bats were least correlated at $d_a = 0.5$ meters, but the correlation rose at $d_a = 3$ meters and decreased with increasing distance. The swallows

were best correlated for $d_a = 1.5$ meters, the correlation decreased for $d_a = 3$ meters and increased with increasing distance. The correlation rate for the untrained fish was fairly level, but increased with increasing metric distance for the trained fish.

The initial comparison indicates that the DRCA is a good basis for studying biological collision avoidance, and future work could be done to further investigate the sensing limitations and priorities of the animals under study. The sensing distance, in terms of both zonal and nearest neighbor models, was shown to have some effect, but additional combinations could be considered to look for a significant trend. Peripheral sensing, the animal's ability to detect obstacles to their sides or behind them, could be characterized through use of a version of the zonal model with cones of varying sizes removed from behind the animal. The static obstacles developed for the current analysis could also be tuned and investigated by varying their size and positioning ($d_{sep,object}$ and γ). Determining the priorities of animals, for example collision avoidance, collective movement, feeding, or landing/resting, will likely always be a challenge, but could help explain results from this and future studies. Although an experimental set-up as controlled as the one used to study hawk moths in the Daniel Lab [Mun13] is not likely possible for vertibrate animals, experiments in a more controlled setting could limit the variables and produce a clearer basis for comparison. Once sufficient data is available, the loop should be closed to improve the engineered systems with the information from the biological species.

BIBLIOGRAPHY

[1] I. Giardina, "Collective behavior in animal groups: Theoretical models and empirical studies," *HFSP Journal*, vol. 2, pp. 205–219, Aug 2008.

[2] S. V. Viscido, J. K. Parrish, and D. Gruenbaum, "The effect of population size and number of influential neighbors on the emergent properties of fish schools," *Ecological Modelling*, vol. 183, pp. 347–363, Apr 2005.

[3] H. Hildenbrandt, C. Carere, and C. Hemelrijk, "Self-organized aerial displays of thousands of starlings: a model," *Behavioral Ecology*, vol. 21, no. 6, pp. 1349–1359, 2010.

[4] P. S. Bhagavatula, C. Claudianos, M. R. Ibbotson, and M. V. Srinivasan, "Optic flow cues guide flight in birds," *Current Biology*, vol. 21, no. 21, pp. 1794–1799, 2011.

[5] Z. Kong, K. Ozcimder, N. Fuller, A. Greco, D. Theriault, Z. Wu, T. Kunz, M. Betke, and J. Baillieul, "Optical flow sensing and the inverse perception problem for flying bats," in *Decision and Control (CDC), 2013 IEEE 52nd Annual Conference on*, (Florence, Italy), December 10-13 2013.

[6] V. Pant and C. Higgins, "Tracking improves performance of biological collision avoidance models," *Biological Cybernetics*, vol. 4-5, pp. 307–322, 2012.

[7] C. W. Reynolds, "Flocks, herds, and schools: A distributed behavioral model," *Computer Graphics*, vol. 21, no. 4, pp. 25–34, 1987.

[8] S. Stienessen and J. Parrish, "The effect of disparate information on individual fish movements and emergent group behavior," *Behavioral Ecology*, vol. 24, no. 5, pp. 1150–1160, 2013. cited By (since 1996)0.

[9] A. B. Kao, N. Miller, C. Torney, A. Hartnett, and I. D. Cousin, "Collective learning and optimal consensus decisions in social animal groups," *PLoS Computational Biology*, vol. 10, no. 8, 2014.

[10] N. O. Handegard, K. M. Boswell, C. C. Ioannou, S. P. Leblanc, D. B. Tjostheim, and I. D. Couzin, "The dynamics of coordinated group hunding and collective information transfer among schooling prey," *Current Biology*, vol. 22, no. 13, pp. 1213–1217, 2012.

[11] D. T. Swain, I. D. Couzin, and N. E. Leonard, "Real-time feedback-controlled robotic fish for behavioral experiments with fish schools," *Proceedings of the IEEE*, vol. 100, no. 1, pp. 150–163, 2012.

[12] B. Chazelle, "Natural algorithms and influence systems," *Communications of the ACM*, vol. 55, no. 12, pp. 101–110, 2012.

[13] B. Chazelle, "An algorithmic approach to collective behavior," *Journal of Statistical Physics*, vol. October, 2014.

[14] S. Karaman and E. Frazzoli, "High-speed flight in an ergodic forest," in *Robotics and Automation (ICRA), 2012 IEEE International Conference on*, (Saint Paul, Minnesota, USA), pp. 2899–2906, May 2012.

[15] M. Hoy, A. S. Matveev, and A. V. Savkin, "Algorithms for collision-free navigation of mobile robots in complex cluttered environments: a survey," *Robotica*, vol. FirstView, pp. 1–35, 10 2014.

[16] J. G. Manathara and D. Ghose, "Reactive collision avoidance of multiple realistic uavs," *Aircraft Engineering and Aerospace Technology*, vol. 83, no. 6, pp. 388–396, 2011.

[17] P. Panyakeow and M. Mesbahi, "Deconfliction algorithms for a pair of constant speed unmanned aerial vehicles," *IEEE Transactions on Aerospace and Electronic Systems*, vol. 50, no. 1, pp. 456–, 2014.

[18] E. Frazzoli, Z.-H. Mao, J.-H. Oh, and E. Feron, "Resolution of conflicts involving many aircraft via semidefinite programming," *Journal of Guidance, Control, and Dynamics*, vol. 24, pp. 79–86, 2001.

[19] B. A. Kumar and D. Ghose, "Radar-assisted collision avoidance/guidance strategy for planar flight," *IEEE Transactions on Aerospace and Electronic Systems*, vol. 37, no. 1, pp. 77–90, 2001.

[20] S. J. Guy, J. Chhugani, C. Kim, N. Satish, M. Lin, D. Manocha, and P. Dubey, "Clearpath: Highly parallel collision avoidance for multi-agent simulation," in *Proc. ACM SIGGRAPH Eurographics Symposium on Computer Animation*, 2009.

[21] E. Lalish and K. Morgansen, "Distributed reactive collision avoidance," *Auton Robot*, vol. 32, pp. 207–226, 2012.

[22] J.-M. Park, D.-W. Kim, Y.-S. Yoon, H. J. Kim, and K.-S. Yi, "Obstacle avoidance of autonomous vehicles based on model predictive control," *Proceedings of the Institution of Mechanical Eningeers, Part D: Journal of Automobile Engineering*, vol. 223, pp. 1499–1515, 2009.

[23] M. A. Ahmadi-Pajouh, F. Towhidkhah, S. Gharibzadeh, and M. Mashhadimalek, "Path planning in the hoppocampo-prefrontal cortex pathway: An adaptive model based receding horizon planner," *Med. Hypotheses*, vol. 68, no. 6, pp. 1411–1415, 2007.

[24] F. Mastrogiovanni, A. Sgorbissa, and R. Zaccaria, "Robust navigation in an unknown environment with minimal sensing and representation," *IEEE Transactions on Systems, Man, and Cybernetics*, vol. 39, pp. 212–229, 2009.

[25] A. Chakravarthy and D. Ghose, "Obstacle avoidance in a dynamic environment: A collision cone approach," *IEEE Transactions on Systems, Man, and Cybernetics - Part A: Systems and Humans*, vol. 28, pp. 562–574, 1998.

[26] P. Fiorini and Z. Shiller, "Motion planning in dynamic environments using velocity obstacles," *International Journal of Robotics Research*, vol. 17, no. 7, pp. 760–772, 1998.

[27] S. A. Kane and M. Zamani, "Falcons pursue prey using visual motion cues: new perspectives from animal-borne cameras," *J Exp Biol*, vol. 217, pp. 225–234, 2014.

[28] K. Ghose, T. K. Horiuchi, P. S. Krishnaprasad, and C. F. Moss, "Echolocating bats use a nearly time-optimalstrategy to intercept prey," *PLOS Biology*, vol. 4, pp. 865–873, 2006.

[29] B. L. Boardman, T. L. Hedrick, D. M. Thierault, N. W. Fuller, M. Betke, and K. A. Morgansen, "Collision avoidance in biological systems using collision cones," in *Proceedings of the American Control Conference*, June 2013.

[30] J. H. Fitch, K. A. S. Jr., and A. U. Shump, "Myotis velifer," in *Mammalian Species*, no. 149, pp. 1–5, American Society of Mammalogists, 1981.

[31] J. Farney and E. D. Fleharty, "Aspect ratio, loading, wing span, and membrane areas of bats," *: Journal of Mammalogy*, vol. 50, pp. 362–367, 1969.

[32] A. P. Moller, "Sexual selection in the barn swallow (hirundo rustica)," *Evolution*, vol. 48, pp. 658–670, June 1994.

[33] K. J. Park, M. Rosén, and A. Hedenström, "Flight kinematics of the barn swallow (hirundo rustica) over a wide range of speeds in a wind tunnel," *Journal of Experimental Biology*, vol. 204, pp. 2741–2750, 2001.

[34] T. L. Hedrick, "Software techniques for two- and three-dimensional kinematic measurements of biological and biomimetic systems," *Bioinspiration & Biomimetics*, vol. 3, no. 3, p. 034001, 2008.

[35] M. Ballerini, N. Cabibbo, R. Candelier, A. Cavagna, E. Cisbani, I. Giardina, V. Lecomte, A. Orlandi, G. Parisi, A. Procaccini, M. Viale, and V. Zdravkovic, "Interaction ruling animal collective behavior depends on topological rather than metric distance: Evidence from a field study," *Proceedings of the National Academy of Sciences*, vol. 105, no. 4, pp. 1232–1237, 2008.

[36] A. Chakravarthy and D. Ghose, "Generalization of the colliison cone approach for motion safety in 3-d enviroments," *Autonomous Robots*, vol. 32, pp. 243–266, 2012.

[37] D. G. Steven V. Viscido, Julia K. Parrish, "Individual behavior and emergent properties of fish schools: a comparison of observation and theory," *Marine Ecology Progress Series*, vol. 273, pp. 239–249, 2004.

Appendix A

QUADRIC SURFACES

Three dimensional cones and spheres fall into the category of quadric surfaces. The basic equation for describing such surfaces is

$$Ax^2 + By^2 + Cz^2 + 2Dxy + 2Eyz + 2Fxz + 2Gx + 2Hy + 2Jz + K = 0 \tag{A.1}$$

and can be represented in matrix form by letting $\mathbf{p} = \begin{bmatrix} x & y & z & 1 \end{bmatrix}^T$ and $Q_{surface}$ be the symmetric matrix

$$Q_{surface} = \begin{bmatrix} A & D & F & G \\ D & B & E & H \\ F & E & C & J \\ G & H & J & K \end{bmatrix}. \tag{A.2}$$

Then (A.1) becomes $\mathbf{p}^T Q_{surface} \mathbf{p} = 0$. Different quadric surfaces can be defined by choosing the appropriate constants $A, B, ..., K$.

A.1 Sphere

The equation for a sphere centered at (a, b, c) with radius r is

$$x^2 + y^2 + z^2 - 2xa - 2by - 2cz + a^2 + b^2 + c^2 - r^2 = 0$$

which translates to constants

$$
\begin{aligned}
&A = B = C = 1 \\
&D = E = F = 0 \\
&G = -a \\
&H = -b \\
&J = -c \\
&K = a^2 + b^2 + c^2 - r^2
\end{aligned}
\qquad \text{or equivalently } Q_{sphere} = \begin{bmatrix} 1 & 0 & 0 & -a \\ 0 & 1 & 0 & -b \\ 0 & 0 & 1 & -c \\ -a & -b & -c & K \end{bmatrix}.
$$

A.2 Cone

The constants for a cone with a vertex at $\mathbf{c}_v = \begin{bmatrix} a & b & c \end{bmatrix}$, cone axis along $\mathbf{c}_a = \begin{bmatrix} d & e & f \end{bmatrix}$, and cone angle α are significantly more complicated than for the sphere. The equation for a double sided cone can be written as the constraint that the vector between the cone vertex and some arbitrary point $\begin{bmatrix} x & y & z \end{bmatrix}$ must always form angle α with the cone axis

$$
\cos\alpha = \frac{(\begin{bmatrix} x & y & z \end{bmatrix} - \mathbf{c}_v) \bullet \mathbf{c}_a}{\| \begin{bmatrix} x & y & z \end{bmatrix} - \mathbf{c}_v\| \cdot \|\mathbf{c}_a\|}. \tag{A.3}
$$

Writing the cone axis as a unit vector $\hat{\mathbf{c}}_a = \mathbf{c}_a / \|\mathbf{c}_a\|$ and squaring to simplify the norm on the right-hand side, this equation can be rewritten as

$$
\left[\left(\begin{bmatrix} x & y & z \end{bmatrix} - \mathbf{c}_v \right)^T \bullet \hat{\mathbf{c}}_a \right]^2 = \left[\left(\begin{bmatrix} x & y & z \end{bmatrix} - \mathbf{c}_v \right)^T \bullet \left(\begin{bmatrix} x & y & z \end{bmatrix} - \mathbf{c}_v \right) \right] \cdot \cos(\alpha)^2.
$$

Substituting in the components of $\mathbf{c}_v$ and $\hat{\mathbf{c}}_a$, the above expression expands to

$$
\begin{aligned}
&a^2d^2 + b^2e^2 + c^2f^2 + 2abde + 2acdf + 2bcef \\
&\quad + d^2x^2 + e^2y^2 + f^2z^2 + 2dexy + 2dfxz + 2efyz \\
&\quad - 2ad(dx + ey + fz) - 2be(dx + ey + fz) - 2cf(dx + ey + fz) = \\
&\qquad\qquad (a^2 + b^2 + c^2 - 2ax - 2by - 2cz + x^2 + y^2 + z^2)\cos(\alpha)^2
\end{aligned}
$$

and grouping like terms and setting equal to zero gives

$$\begin{aligned}(d^2-\cos(\alpha)^2)x^2+(e^2-\cos(\alpha)^2)y^2+(f^2-\cos(\alpha)^2)z^2\\ +(2a\cos(\alpha)^2-2ad^2-2bed-2cdf)x\\ +(2b\cos(\alpha)^2-2ade-2be^2-2cfe)y\\ +(2c\cos(\alpha)^2-2adf-2bef-2cf^2)z\\ +(2de)xy+(2df)xz+(2ef)yz\\ +a^2d^2+b^2e^2+c^2f^2+2abde+2acdf+2bcef\\ -a^2\cos(\alpha)^2-b^2\cos(\alpha)^2-c^2\cos(\alpha)^2=0.\end{aligned}$$

Comparing the components to the coefficients in (A.1), the terms to describe the cone matrix Q_{cone} are easily found to be

$$\begin{aligned}A&=d^2-\cos(\alpha)^2\\ B&=e^2-\cos(\alpha)^2\\ C&=f^2-\cos(\alpha)^2\\ D&=de\\ E&=ef\\ F&=df\\ G&=a\cdot\cos(\alpha)^2-d(ad+be+cf)\\ H&=b\cdot\cos(\alpha)^2-e(ad+be+cf)\\ J&=c\cdot\cos(\alpha)^2-f(ad+be+cf)\\ K&=a^2d^2+b^2e^2+c^2f^2+2abde+2acdf+2bcef-a^2\cos(\alpha)^2-b^2\cos(\alpha)^2-c^2\cos(\alpha)^2,\end{aligned}$$

where the matrix is populated as in (A.2).